



Multidimensional carbon-based polymer/Bi₂O₂CO₃ S-scheme heterojunction boosting carrier separation in efficient photocatalytic seawater purification

Shihao Jia^{a,1}, Huimin Han^{a,1}, Bin Wang^{b,d,*}, Jinyuan Liu^{b,d}, Qi Tang^a, Gaopeng Liu^b, Qingdong Ruan^d, Xingwang Zhu^{c,**}, Huaming Li^b, Chongtai Wang^a, Paul K. Chu^d, Yingjie Hua^{a,**}

^a School of Chemistry and Chemical Engineering of Hainan Normal University, Key Laboratory of Electrochemical Energy Storage and Energy Conversion of Hainan Province, Key Laboratory of Electrochemical Energy Storage and Light Energy Conversion Materials of Haikou City, Haikou 571158, PR China

^b School of Chemistry and Chemical Engineering, Institute for Energy Research, Jiangsu University, Zhenjiang 212013, PR China

^c School of Environmental Science and Engineering, College of Mechanical Engineering, Yangzhou University, Yangzhou 225009, PR China

^d Department of Physics, Department of Materials Science and Engineering, and Department of Biomedical Engineering, City University of Hong Kong, Kowloon, Hong Kong, China

ARTICLE INFO

Keywords:

Bi₂O₂CO₃
Carbon polymer quantum dots
g-C₃N₄
S-scheme heterojunctions
Photocatalytic seawater purification

ABSTRACT

Photocatalytic decomposition of seawater pollutants using solar energy as driving force has far-reaching significance. Herein, the multidimensional carbon-based polymer/Bi₂O₂CO₃ (BOC) S-scheme heterojunction, including: 2D graphitic carbon nitride/3D peony flower-like BOC composite and 0D carbon polymer dots/2D ultra-thin BOC nanosheets composite, were successfully constructed. Under light excitation, the photogenerated electrons of BOC recombine with the holes of the carbon-based polymer via S-scheme heterojunction, effectively maintaining the high redox properties of the photogenerated electrons for carbon-based polymer and the holes for BOC. The 1 wt% CPDs/BOC shows the best photocatalytic performance, with a homemade wastewater treatment device, heavily polluted (20 L of 100 mg/L RhB) seawater can be purified with only 5 hours of sunlight exposure. Meanwhile, the toxicology of intermediate products during the photocatalytic degradation process was analyzed in detail. Using the purified solution to cultivate bean sprouts found that the development of bean sprouts was not inhibited.

1. Introduction

With rapid globalisation and urbanisation, organic dyes and antibiotics with potent inhibitory properties against pathogenic bacteria are widely used [1–3]. However, if wastewater containing significant amounts of these compounds is not adequately treated, it can pose a threat to the natural water body environment, with the oceans being particularly affected [4–6]. Therefore, addressing the degradation of persistent organic dyes and antibiotics in marine ecosystems is crucial. Photocatalysis is a commonly used technique for safe, efficient, and sustainable water purification [7,8]. However, research on photocatalysis for marine wastewater treatment is limited. This is due to

reasons such as the low efficiency of photocatalyst charge separation, limited active species, and unknown degradation performance in complex environments [9].

To overcome the limitations of photocatalysts, researchers have explored strategies such as the introduction of defects, controlling the morphology, incorporation of co-catalysts like noble metals and formation of heterojunctions [10–13]. Among these methods, the construction of heterojunctions stands out due to its significant responsiveness to visible light, efficient charge separation, and potent redox activity. In light of the limitations associated with traditional type-II and Z-scheme heterojunctions, a novel S-scheme heterojunction has emerged as a promising alternative. This innovative photocatalytic

* Corresponding author at: School of Chemistry and Chemical Engineering, Institute for Energy Research, Jiangsu University, Zhenjiang 212013, PR China.

** Corresponding authors.

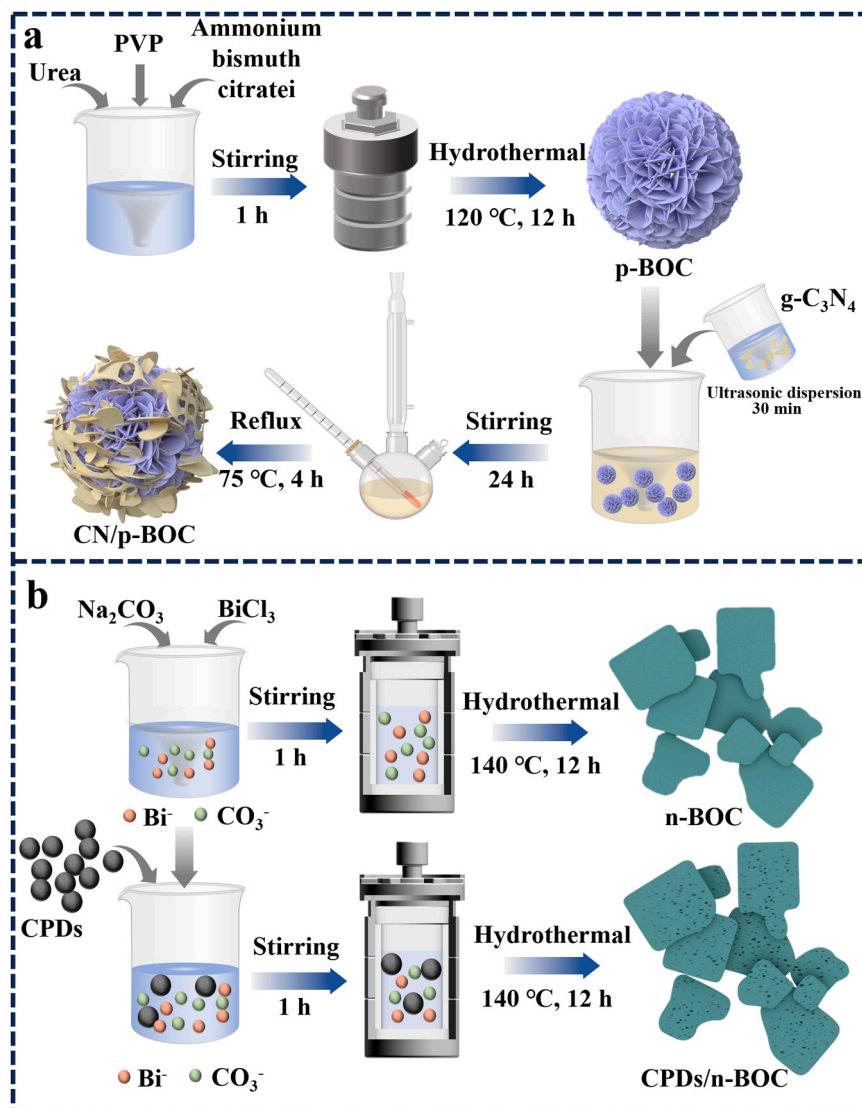
E-mail addresses: wangbin@ujs.edu.cn (B. Wang), zxw@yzu.edu.cn (X. Zhu), 521000hua282@sina.com (Y. Hua).

¹ These authors contributed equally to this work.

structure integrates oxidation photocatalysts (OP) and reduction photocatalysts (RP) [14,15]. To address the disparity in Fermi level (E_f) at the interface, electrons from RP are transferred to OP, resulting in RP acquiring a positive charge and causing its band structure to bend upwards. Conversely, OP gains electrons, becoming negatively charged, thereby causing its band structure to bend downwards and generating an internal electric field pointing from RP to OP. Facilitated by this intrinsic electric field and Coulombic forces, the excess electrons in OP rapidly recombine with the surplus holes in RP. This process enables effective separation of holes in OP and electrons in RP [16,17]. Consequently, the S-scheme heterojunction demonstrates enhanced photocatalytic efficacy and effectively mitigates the reverse reaction. Although BP/BiOBr, CdLa₂S₄/ZnIn₂S₄, N-ZnO/g-C₃N₄, and Bi₂WO₆/g-C₃N₄, have been developed [18–21], most of them face the following challenges: (1) absence of chemical bond-level interfacial interactions and reduced charge transfer efficiency and stability and (2) complex synthetic processes and use of expensive or toxic raw materials boding ill for suitability and large-scale production [22]. As a result, there is a pressing need to develop environmentally friendly, cost-effective, and easily synthesized S-scheme heterojunction photocatalyst.

BOC is a representative Aurivillius compound characterized by its unique layered structure, non-toxic properties, and excellent stability [23–25]. While it serves as a suitable photocatalyst for pollutant

removal, it possesses inherent limitations, including suboptimal utilization of visible light ($\lambda \leq 450$ nm) and a high likelihood of electron-hole recombination, which can compromise catalytic efficiency [26,27]. Therefore, it is crucial to search for excellent photocatalysts that can match the band structure of BOC to construct S-scheme heterojunctions. Carbon-based polymers have attracted increasing attention as photocatalysts on account of their inherent physical and chemical properties [28]. In particular, g-C₃N₄ (CN) has a unique electronic structure and surface characteristics, making it promising in pollutant degradation and renewable energy generation [29,30]. Furthermore, the 2D structure of CN enables the formation of favorable interfaces with other semiconductors. In addition to CN, carbon polymer dots (CPDs) is an emerging carbon-based polymeric materials by offer several advantages including fluorescence, biocompatibility, non-toxicity, and easy synthesis thus boding well for photocatalysis, bioimaging, drug delivery, and chemical sensing [31,32]. Their robust fluorescence characteristics enable them to efficiently absorb visible light to promote the photocatalytic reactions [33]. Consequently, the integration of CPDs with other semiconducting photocatalysts such as PbBiO₂Br, and CN can create heterojunctions for efficient photocatalytic reactions [34,35]. However, research of CPDs is still in the early stage and the pertinent photocatalytic mechanisms and properties are not well understood. Composite construction of S-scheme heterojunctions by combining BOC



Scheme 1. Schematic illustration of the synthesis of (a) CN/p-BOC and (b) CPDs/n-BOC.

with a good carbon-based polymer matching its band structure, holds the promise of enhancing the separation efficiency of photogenerated charge carriers, maintaining high redox capability, and increasing the concentration of active oxygen species.

In this study, novel S-scheme heterojunction of carbon-based polymer/BOC was rationally designed and constructed for seawater purification. The novel S-scheme heterojunctions, denoted as 2D/3D CN/peony flower-like BOC (CN/p-BOC), was synthesized through electrostatic adsorption and condensation reflux (Scheme 1a). The optimized ratio of the CN/p-BOC composite (10 wt% CN/p-BOC) exhibited degradation properties 2.77, 2.27, and 2.87 times higher than pristine p-BOC for RhB, TC, and CIP, respectively. However, this synthesis method is cumbersome, on the basis of which another innovative S-scheme heterojunction, 0D/2D CPDs/BOC nanosheets (CPDs/n-BOC), was constructed using a simpler in situ hydrothermal technique (Scheme 1b). Significantly, the photocatalytic degradation performance of 1 wt% CPDs/n-BOC surpassed that of 10 wt% CN/p-BOC, exhibiting improvements of 2.7, 2.1, and 1.50 times for RhB, TC, and CIP, respectively. Under visible light, the e^- in the CB of BOC would readily recombine with the h^+ in the VB of carbon-based polymer, following an S-scheme charge migration pathway. This result is supported by theoretical calculations as well as experimental characterizations such as XPS, KPFM, and photodeposition. The composites also maintain this good photocatalytic activity in seawater environment, which may be attributed to their good resistance to ionic interference. Toxicological modeling simulations and bean sprout growth tests for the photocatalytic degradation products revealed their almost non-toxic nature. Consequently, a medium-volume natural light-driven wastewater treatment device was developed based on the most efficient catalyst in this study. This work presents a novel idea for the future realization of seawater purification through photocatalysis.

2. Experimental section

2.1. Materials and synthesis

The natural seawater (simple filtration only) was obtained from the Southern China Sea (Haikou, China). Ammonium bismuth citrate ($C_6H_{13}BiN_2O_7 \cdot H_2O$), bismuth trichloride ($BiCl_3$), sodium carbonate ($NaCO_3$), sodium chloride ($NaCl$), sodium Sulfate (Na_2SO_4), sodium bromide ($NaBr$), sodium bicarbonate ($NaHCO_3$), potassium chloride (KCl), ammonium chloride (NH_4Cl), calcium chloride ($CaCl_2$), magnesium chloride ($MgCl_2$), citric acid, ethylenediamine and polyvinylpyrrolidone (PVP) were purchased from Shanghai Macklin Biochemical Co. Hexadecyltrimethylammonium bromide (CTAB), urea (CH_4N_2O), methenamine (HMT), ethylenediamine (EDA), and ethanol (EtOH) were obtained from Sinopharm Chemical Reagent Co. All the reagents were used directly and the solutions were prepared with deionized water.

2.1.1. Synthesis of peony flower-like BOC

The peony flower-like BOC (p-BOC) was synthesized by a hydrothermal method. Solution A was prepared by combining 2 mmol ammonium bismuth citrate and 10 mmol urea in deionized water, followed by stirring at 800 rpm for one hour. Subsequently, 600 mg of PVP were dissolved in solution A, sealed inside a Teflon-line autoclave (100 mL), and heated to 120 °C for 12 hours. The product was centrifuged, washed with deionized water and ethanol several times, and dried for 12 h to obtain the p-BOC.

2.1.2. Synthesis of 2D ultra-thin BOC nanosheets

In the standard synthesis, 35 mL of ethanol and 2 mL of deionized water were mixed and stirred vigorously (800 rpm). 300 mg of CTAB were dissolved and then 300 mg of HMT were added and stirred until the solution became transparent. 1 g of $BiCl_3$ and 600 mg of Na_2CO_3 were added to the solution and stirred vigorously (800 rpm) for 1 h.

Afterward, the mixture was placed in a 50 mL Teflon-line autoclave and heated to 140 °C for 12 h. The product was collected by centrifugation, washed with water and ethanol several times, and dried to obtain the 2D ultra-thin BOC nanosheets (n-BOC).

2.1.3. Synthesis of g- C_3N_4

Place urea (10 g) in a crucible (50 mL). In a muffle furnace, the temperature was increased to 550 °C for 4 hours. White fluffy two-dimensional CN was obtained.

2.1.4. Synthesis of CPDs

The CPDs was prepared hydrothermally according to the literature [31]. 5 mmol citric acid and 335 μ L of ethylenediamine were dissolved in 10 mL of deionized water. After stirring for 30 minutes, the solution was transferred to a 25 mL Teflon-lined reactor, and heated to 200 °C for 5 h. After the reactor cooled to room temperature, the product was dialyzed for 24 h to obtain the CPDs solution and then freeze-dried to obtain the solid CPDs.

2.1.5. Synthesis of CN/p-BOC

A given amount of CN was placed in a water-methanol solution and sonicated for 30 min to achieve complete dispersion. p-BOC was introduced to the suspension, stirred magnetically for 24 h, and refluxed for 4 h at 75 °C under continuous stirring (500 rpm). After the evaporation of methanol and water, the CN/p-BOC photocatalyst was obtained after drying overnight at 60 °C under vacuum.

2.1.6. Synthesis of CPDs/n-BOC

The one-pot protocol was adopted for the synthesis of CPDs/n-BOC. In the standard synthesis, 35 mL of ethanol and 2 mL of deionized water were mixed and stirred and 300 mg of CTAB were added and dissolved. 300 mg of HMT were added and stirred until the solution became transparent. 1 g pf $BiCl_3$, 600 mg of Na_2CO_3 , and a given amount of CPDs were dissolved and stirred (800 rpm) for 1 h. The mixture was transferred to a 50 mL Teflon-line autoclave and heated to 140 °C for 12 h. The product was collected by centrifugation, washed with water and ethanol several times, and dried to obtain CPDs/n-BOC.

2.2. Materials characterization

Scanning electron microscopy (SEM) was conducted on the JEOL JSM-7100 F and transmission electron microscopy (TEM) provided more information. Fourier transform infrared (FTIR) spectroscopy was performed on the Nicolet Nexus 470 and X-ray diffraction (XRD) was done on the Shimadzu XRD-6000. X-ray photoelectron spectroscopy (XPS) was carried out on the VG MultiLab 2000 instrument and UV-visible diffuse reflectance spectroscopy (DRS) was conducted in the wavelength range of 200–800 nm. The steady-state photoluminescence (PL) spectra were collected on the QuantaMaster and TimeMaster fluorescence spectrophotometers. The surface photovoltage (SPV) was determined on the Zolihan, SR830. Electrochemical impedance spectroscopy (EIS), Electrochemical active surface area (ECSA) and photocurrent measurements were performed using a conventional three-electrode system on the Chenhua CHI 660B. Electron spin resonance (ESR) spectroscopy was carried out on the Bruker model ESR JES-FA200 spectrometer. The surface potentials of samples under dark and light irradiation ($\lambda > 400$ nm) conditions were measured using the Kelvin probe force microscope (KPFM) equipped in a scanning probe microscope (SPM) system (Bruker Dimension icon, Germany).

2.3. DFT calculation

The DFT calculation was performed in the Vienna ab initio simulation package (VASP). The spin-polarized GGA PBE functional [36], all-electron plane-wave basis sets with an energy cutoff of 520 eV, and projector augmented wave (PAW) method were adopted [37,38]. A ($3 \times$

3×1) Monkhorst-Pack mesh was used for the Brillouin-zone integration to be sampled. The conjugate gradient algorithm was used for optimization. The convergence threshold was set to 1×10^{-5} eV in total energy and 0.02 eV/Å in force for each atom.

2.4. Photocatalytic experiments

The photocatalytic degradation properties of the samples were investigated with the aid of three model pollutants RhB, TC, and CIP. The initial concentrations were 10 mg/L for RhB and 15 mg/L for both CIP and TC. A 300 W xenon lamp was placed in the photocatalytic reactor and the light was filtered for $\lambda > 400$ nm. The temperature was controlled during photocatalytic degradation using a constant-temperature water circulation system. Initially, the photocatalyst (30 mg) was added to 100 mL of the solution of the pollutant. Before photocatalytic degradation, the suspension was stirred in the dark for 30 minutes to reach an equilibrium between adsorption and desorption. The lamp was then turned on and at specified time intervals, 4 mL of the suspension were collected and centrifuged. Finally, the absorbance of RhB, TC, and CIP was measured separately at 554 nm, 358 nm, and 276 nm by UV-visible spectrophotometry. The total organic carbon (TOC) remaining of actual sewage was studied by a TOC analyzer (Shimadzu TOC-L).

3. Results and discussion

3.1. Structure and morphology

The morphology and microstructure of the photocatalyst are examined by TEM and HR-TEM. As shown in Fig. 1a, the pure p-BOC has a 3D peony flower ball-like structure with a rough surface and a diameter of about 1.3 μm . Fig. 1b shows that CN has the typical layer structure with one or a few layers of stacked graphite. Fig. 1c shows the morphology of 10 wt% CN/p-BOC and the 3D p-BOC is enveloped by a 2D CN layer. The HRTEM images in Fig. 1d-e reveal wrapped CN on p-BOC with close interfaces between CN and p-BOC. The lattice spacing of 0.27 observed from CN/p-BOC corresponds to the (110) plane of p-BOC consistent with XRD (Fig. 2a). The CN wrapped in the outer layer of BOC is amorphous. This structure facilitates the formation of heterostructures which ultimately enhance the transfer of photogenerated carriers and boost the photocatalytic activity.

The TEM and HR-TEM images of n-BOC, CPDs, and CPDs/n-BOC are depicted in Fig. 1f-i. Fig. 1f reveals the 2D sheet-like shape of n-BOC and the HR-TEM images confirm a lattice spacing of 0.295 nm (Fig. 1f inset), which corresponds to the (013) crystal plane of n-BOC. CPDs have a 0D dot-like morphology with diameters between 3 and 5 nm in Fig. 1g. The HR-TEM images indicate a lattice spacing of 0.211 nm (Fig. 1g inset) that can be indexed to the (100) crystal plane of CPDs. The CPDs are

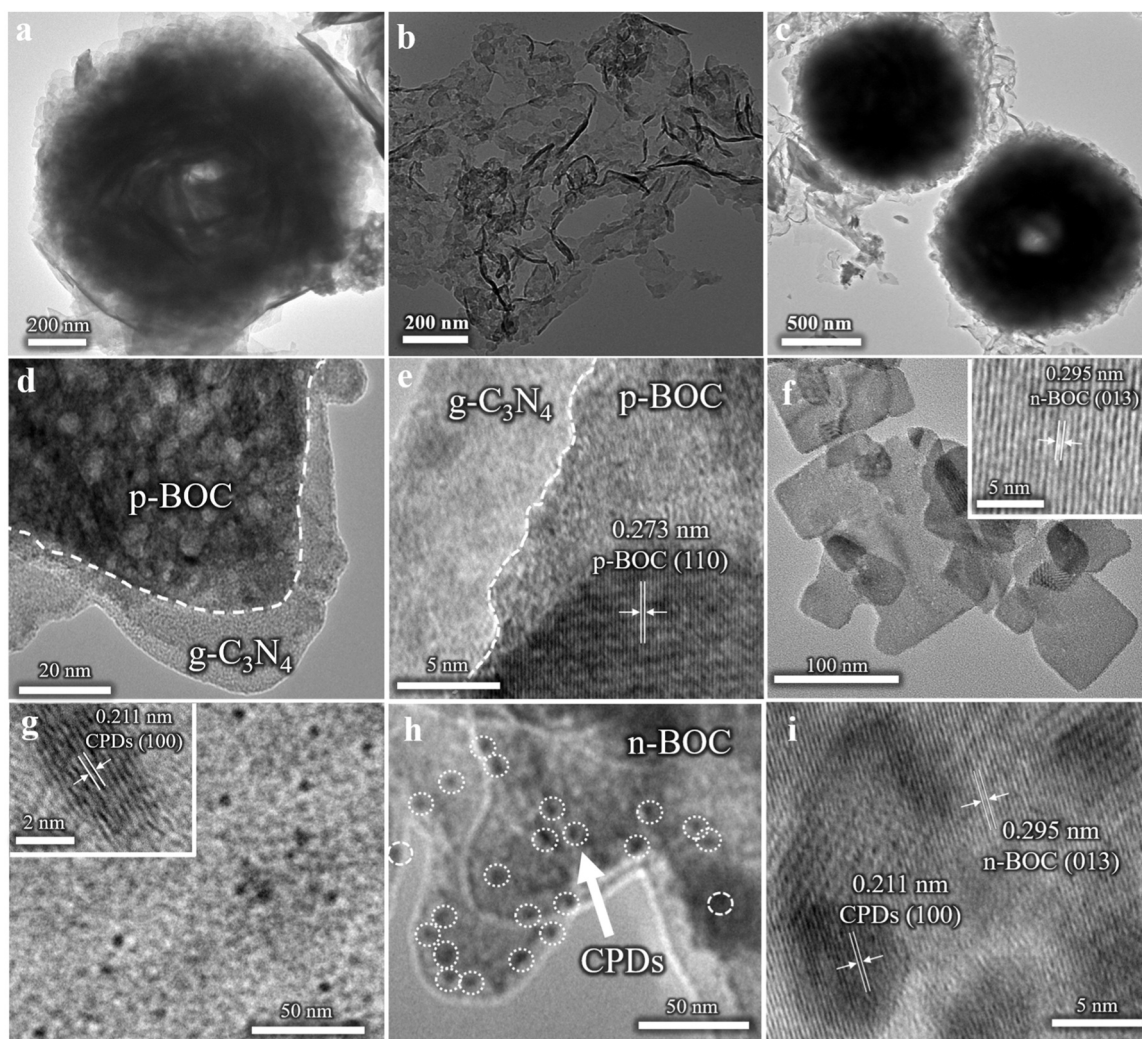


Fig. 1. TEM image of (a) p-BOC, (b) CN, and (c) 10 wt% CN/p-BOC; (d-e) HR-TEM images of 10 wt% CN/p-BOC; TEM and HR-TEM images of (f) n-BOC, (g) CPDs, and (h-i) 1 wt% CPDs/n-BOC.

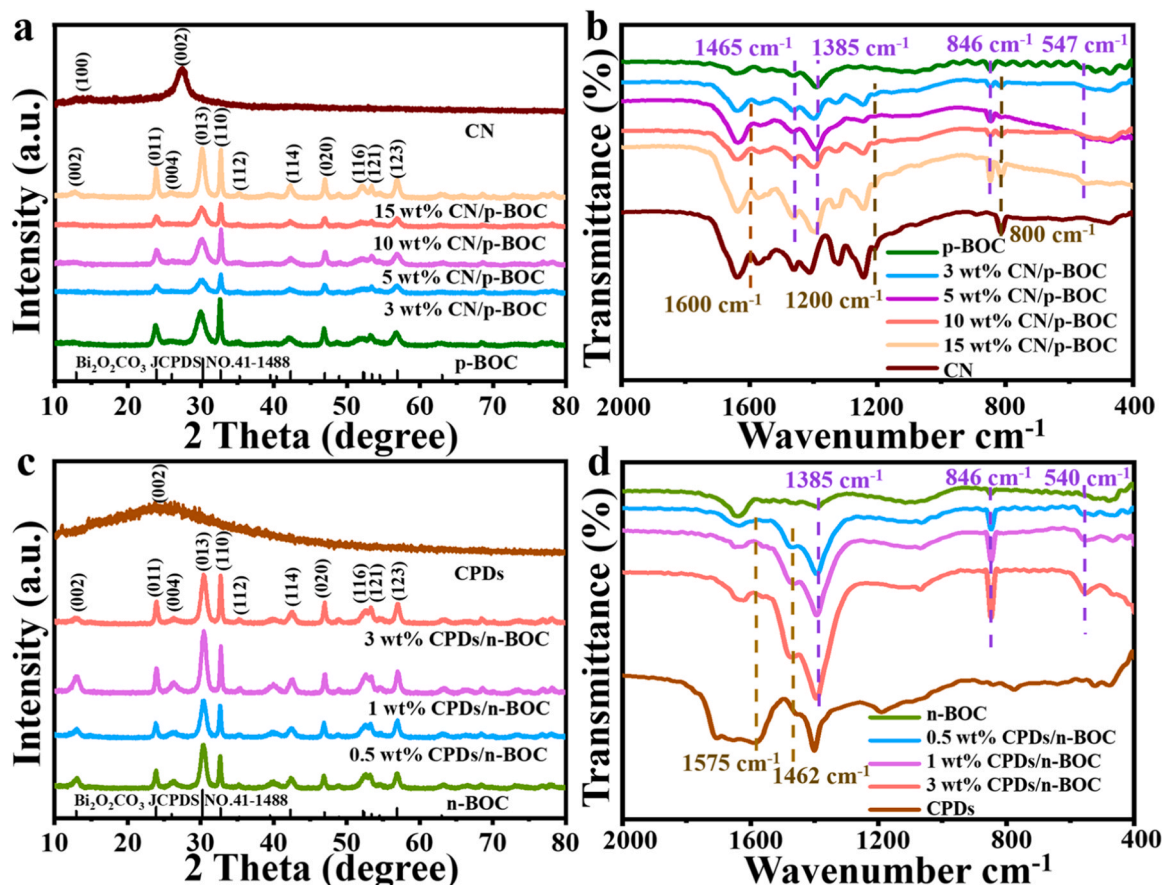


Fig. 2. (a) XRD patterns and (b) FTIR spectra of p-BOC, CN and CN/p-BOC; (c) XRD patterns and (d) FTIR spectra of n-BOC, CPDs and CPDs/n-BOC.

distributed on the surface of n-BOC as shown in Fig. 1h. Fig. 1i reveals lattice spacings at 0.211 nm and 0.295 nm consistent with the (100) crystal plane of CPDs and (013) crystal plane of BOC, respectively, thus confirming the successful preparation of the CPD/n-BOC composite. The combination of CPDs and n-BOC provides the ideal conditions for the formation of S-scheme heterojunctions.

The specific surface area was determined based on the nitrogen adsorption-desorption isotherm (Fig. S1). The specific surface areas of p-BOC, CN, and CN/p-BOC (3, 5, 10, 15 wt%) are 33.32, 26.38, 37.56, 50.48, 83.21, and 71.54 m^2/g , respectively. The 10 wt% CN/p-BOC has a significantly larger specific surface area than pure p-BOC showing a maximum increase of 2.5 times. This increase is ascribed to enhanced intercalation of the 2D CN and p-BOC composite. CPDs/n-BOC also has a larger specific surface area than the monomeric n-BOC. Specifically, n-BOC and CPDs/n-BOC (0.5, 1, 3 wt%) have specific surface areas of 15.85, 17.79, 22.81, and 22.93 m^2/g , respectively. Interestingly, the specific surface area of 1 wt% CPDs/BOC is only 1.4 times larger than that of the monomer due to the limited impact of the small amount of CPDs on the specific surface area of CPDs/BOC. A larger specific surface area is expected to lead to more exposed active sites and better photocatalytic activity [39].

The crystal structure is analyzed by XRD. As shown in Fig. 2a, CN exhibits diffraction peaks from the (100) and (002) planes at $2\theta = 13.0^\circ$ and 27.4° . The diffraction peaks from the monomeric p-BOC and CN/p-BOC match the standard diffraction data of tetragonal $\text{Bi}_2\text{O}_2\text{CO}_3$ (JCPDS card no. 41-1488), confirming the formation of the tetragonal $\text{Bi}_2\text{O}_2\text{CO}_3$ phase. To further verify the presence of CN in the x wt% CN/BOC samples, FTIR spectra are acquired from BOC, CN, and x wt% CN/BOC (Fig. 2b). The peaks from CN appear at 1600 and 800 cm^{-1} . The strong peak at 800 cm^{-1} arises from out-of-plane bending of the s-triazine unit, while several strong peaks in the 1200–1600 cm^{-1} region are the typical

stretching vibrations of heptazine [40]. These findings confirm the presence of CN in the samples. Peaks at 1465, 1385, 846, and 547 cm^{-1} are also observed from of p-BOC in the infrared spectrum of CN/p-BOC [41]. The peak at 1385 cm^{-1} exhibits a partial blue shift, indicating an interaction between CN and BOC attributable to the asymmetric vibration ν_3 mode of CO_3^{2-} .

The phase structures of CPDs, n-BOC, and CPDs/n-BOC are determined by XRD. As shown in Fig. 2c, CPDs show a broad diffraction peak at approximately 24° , consistent with the (002) crystal plane of graphite typical of amorphous carbon [39,42]. In contrast, n-BOC and the composite materials exhibit XRD diffraction peaks corresponding to the tetragonal-phase BOC, with no distinct CPDs characteristic peaks observed due to the smaller CPDs concentration. Fig. 2d shows a peak at 540 cm^{-1} associated with Bi-O stretching from both the pure n-BOC and CPDs/n-BOC [30]. Additionally, the peaks at 1575 and 1462 cm^{-1} stem from —C=N and —N—H in CPDs, confirming the presence in CPDs/n-BOC [34]. These analyses corroborate the incorporation and interaction of p-BOC and CN as well as n-BOC and CPDs, potentially forming the CN/p-BOC and CPDs/n-BOC heterojunctions.

3.2. S-scheme mechanism

XPS is employed to determine the chemical composition and chemical valence states of the materials [43]. As shown in Fig. S2a, the XPS spectrum of p-BOC shows the peaks of Bi, C, and O, but the N peak is less pronounced due to the smaller concentration. In contrast, the 10 wt% CN/p-BOC composite shows more N because of the introduction of CN. However, the N content in the CPDs incorporated into n-BOC is relatively modest (Fig. S2b) and the N peak is less prominent in the spectrum of 1 wt% CPDs/BOC. Fig. 3a shows peaks at 158.7 eV and 164.1 eV corresponding to Bi^{3+} in p-BOC [44]. The peaks of Bi 4 f of

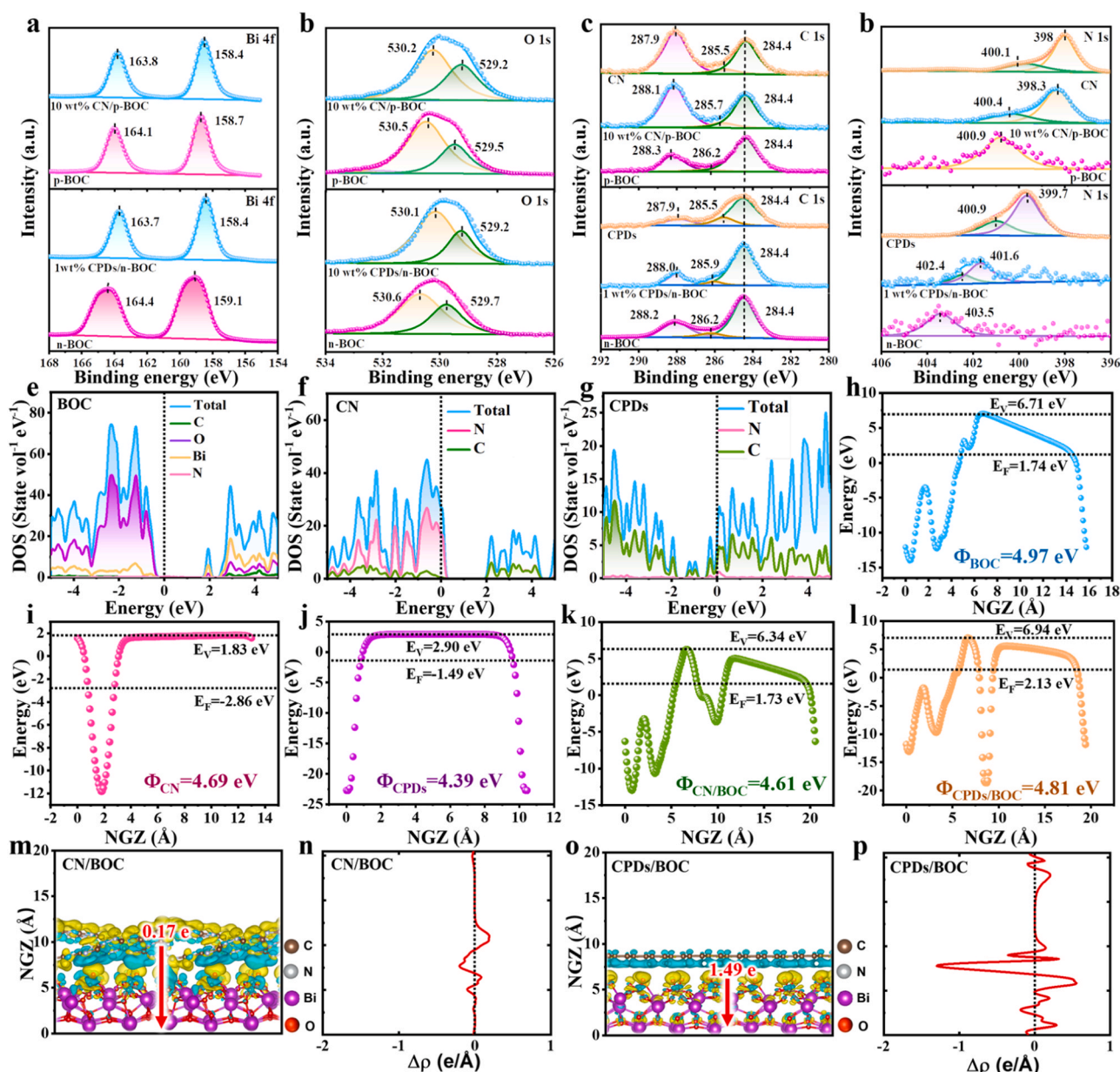


Fig. 3. XPS survey spectra: (a) Bi 4f, (b) O 1s, (c) C 1s, and (d) N 1s; Calculated DOS of (e) BOC, (f) CN, and (g) CPDs; Calculated work functions of (h) BOC, (i) CN, (j) CN/BOC (k) CPDs, and (l) CPDs/BOC. (m, o) Electronic structure changes of CN/BOC models and CPDs/BOC models. (n, p) Calculated charge density difference.

10 wt% CN/p-BOC to smaller binding energies by 0.7 eV and the peaks at 159.1 and 164.4 eV arise from Bi^{3+} in n-BOC [45]. The Bi 4f peaks of 1 wt% CPDs/n-BOC also shift to smaller binding energies of 0.3 eV. As shown by the O 1s spectrum (Fig. 3b), the Bi-O bonds in $[\text{Bi}_2\text{O}_2]^{2+}$ and surface-adsorbed $\text{H}_2\text{O}/\text{OH}^-$ are observed at 529.5 eV and 530.5 eV, respectively [46]. A negative shift of 0.3 eV is observed from 10 wt% CN/p-BOC and similarly, the peaks of CPDs/n-BOC exhibit a negative shift of 0.5 eV. As shown in the C 1s spectra (Fig. 3c), the peak at 284.4 eV serves as the reference, and the peaks at binding energies of 287.9 eV (CN) and 288.3 eV (p-BOC) are associated with sp^2 carbon in CN and carbonate ions in BOC, respectively [47]. The peaks at binding energies of 285.5 eV (CN), 286.2 eV (p-BOC), and 285.7 eV (10 wt% CN/p-BOC) are from carbon impurities [48]. In comparison with p-BOC, the C 1s binding energy of 10 wt% CN/p-BOC shows a negative shift. The peak at 287.9 eV can be assigned to sp^2 or sp^3 carbon in CPDs and the peak at 288.2 eV of n-BOC corresponds to C in CO_3^{2-} [30]. Similarly, the C 1s binding energy of 1 wt% CPDs/n-BOC shows a negative shift compared to n-BOC. As shown in the N 1s spectrum (Fig. 3d), the N in

p-BOC exhibited an oxidized state. In the CN/p-BOC composite, compared to pure CN, $\text{C}=\text{N}-\text{C}$ and $\text{C}-\text{N}-\text{C}$ in CN display positive shifts. The nitrogen peaks of n-BOC are discernible due to HMT and CTAB in the starting materials. The N 1s peak of 1 wt% CPDs/n-BOC exhibits a positive shift compared to CPDs but a negative shift in comparison with n-BOC. These results confirm the close contact between the carbon-nitrogen polymer and BOC, which facilitates electron transfer between them.

DOS calculations are performed to investigate the band composition and hybrid states, as illustrated in Fig. 3e-g. In the BOC, the VB is primarily composed of O 2p orbitals, while the CB consists mainly of Bi 6p orbitals. As for CN, the VB is primarily composed of N 5p orbitals, and the CB includes C 2p orbitals. In contrast, both the VB and CB of CPDs are composed of C 5d orbitals. As shown in Fig. 3h-j, the estimated work functions of BOC, CN, and CPDs are 4.97 eV, 4.69 eV, and 4.39 eV, respectively. The differences in the work functions indicate the presence of charge transfer at the CN/BOC and CPDs/BOC interfaces. When the heterojunctions are established, electrons tend to migrate from the

carbon polymers (CN and CPDs) to BOC to achieve Fermi-level equilibrium. The estimated work functions of CN/BOC and CPDs/BOC after equilibrium are 4.61 eV and 4.81 eV, respectively (Fig. 3k-i). Fig. 3m and o illustrate the charge density differences calculated by DFT, highlighted by yellow and cyan regions respectively. The yellow part indicates an increase in charge density and the cyan part indicates a decrease in charge density. These images depict that carbon-based polymers (CN and CPDs) predominantly lose electrons at the interfaces while accumulating electrons near the BOC interfaces. Bader charge analysis reveals that CN transfers approximately 0.17 electrons to the BOC layer, whereas CPDs transfer about 1.49 electrons to the BOC layer. Fig. 3n and p display the plane-averaged charge density difference along the z-axis direction, where positive values denote electron accumulation and negative values denote electron enrichment. This observed change in charge at the interface signifies the flow of electrons from the carbon-based polymers (CN and CPDs) across the interfacial surface of the heterojunction into the BOC side, consequently establishing a built-in electric field. Consequently, under the influence of this built-in electric field, the photogenerated electrons in the conduction band of the photoexcited BOC are transferred to combine with holes in the valence

band of the carbon polymer, leaving behind electrons (e^-) and holes (h^+) with high reduction and oxidation potentials, respectively. This indicates that the carbon-based polymer/BOC conforms to the carrier transfer mechanism of an S-scheme heterojunction.

The light-absorbing properties of the materials are investigated by UV-visible diffuse reflectance spectroscopy. As shown in Fig. 4a, the optical absorption edges of p-BOC and CN are nearly 325 and 445 nm, respectively. All the CN/p-BOC samples exhibit noticeable redshifts in the absorption edges compared to pure p-BOC, indicating an extended range of visible light absorption. The intrinsic optical absorption edge of pure p-BOC occurs at 450 nm, and the shift in the absorption edge of the composites is shown by the brown-black color of CPDs (Fig. 4b). To determine the bandgaps (E_g) of p-BOC, n-BOC, and CN monomers, the formula: $ah\nu = A(h\nu - E_g)^n$ is used, where α represents the absorption coefficient, $h\nu$ corresponds to photon energy, and n is a constant [49]. According to the classical Tauc method, plotting $(\alpha E_{\text{photon}})^{1/2}$ against E_{photon} (Fig. 4c) shows bandgaps of 2.26 eV, 2.39 eV, and 2.61 eV for p-BOC, n-BOC, and CN, respectively [50,51]. Given that both BOC and CN exhibit N-type semiconductor characteristics, where the CB aligns with the flat-band potential, the VB positions of p-BOC, n-BOC, and CN

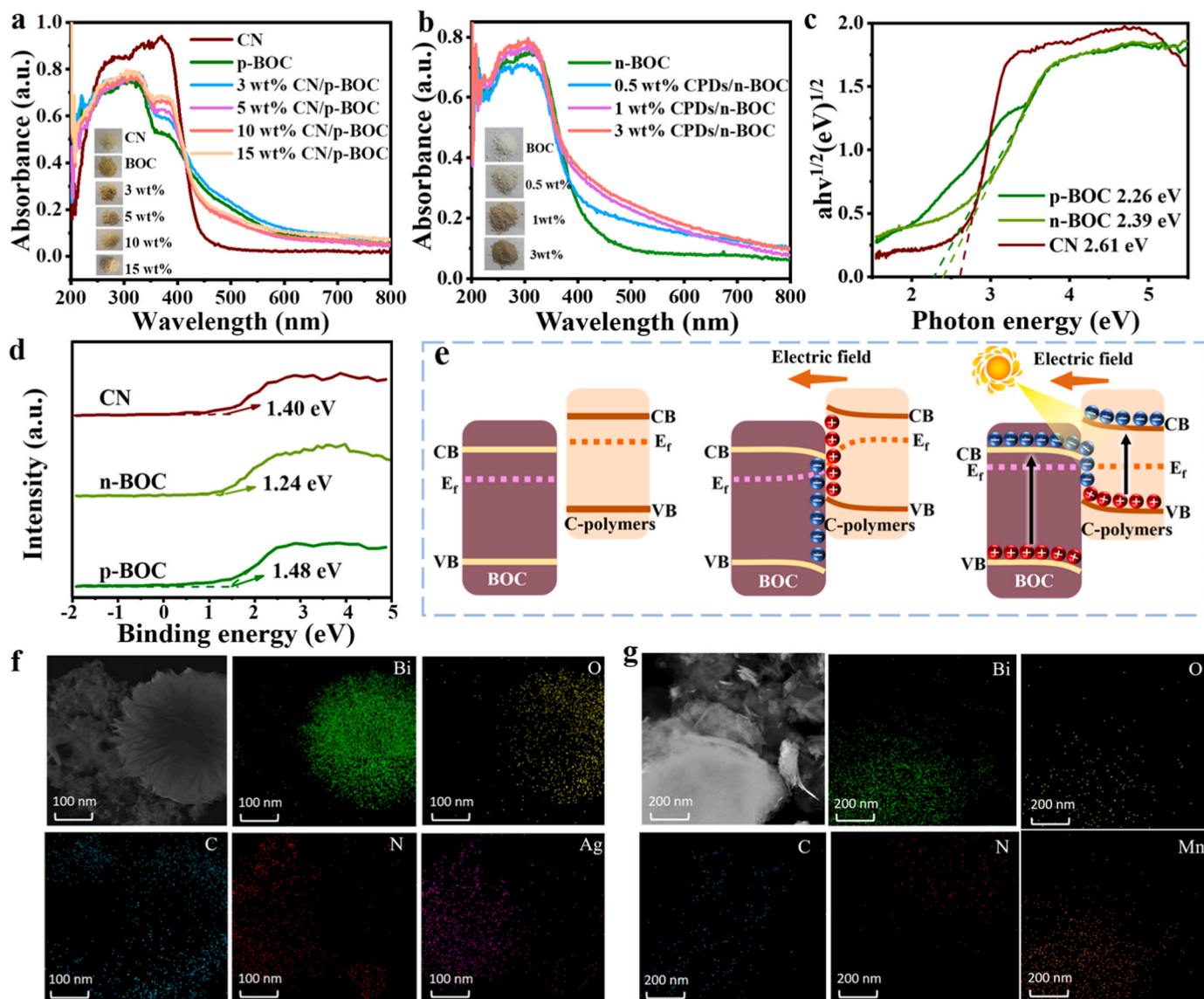


Fig. 4. (a-b) UV-vis DRS of the samples; (c) Bandgaps of the samples; (d) VB-XPS images of the samples; (e) Energy band diagram of the carbon polymers and BOC before and after contact together with the photo-induced carrier migration mechanism; TEM elemental maps of (f) 10 wt% CN/BOC photodeposited with Ag and (g) 10 wt% CN/BOC photodeposited with MnO_x.

are 1.48 eV, 1.24 eV, and 1.40 eV (Fig. 4d), respectively, based on the VB-XPS measurements. Consequently, the CB positions of p-BOC, n-BOC, and CN are -0.78 eV, -1.15 eV, and -1.21 eV, respectively. Based on previous work, the band gap energy for CPDs is 0.67 eV, and the CB and VB positions are -1.23 eV and -0.56 eV, respectively [34].

Accordingly, a modified electron transfer pathway is proposed (Fig. 4e). Owing to the close contact between BOC and carbon polymers, electrons in the carbon polymers migrate spontaneously to BOC across the interface to achieve an equilibrium at the Fermi levels. As a result, the carbon polymers lose electrons and acquire positive charges, while BOC gains electrons leading to a negative charge. This process generates an internal electric field at the interface. Simultaneously, because of electron loss, the band edges of the carbon polymers bend upward, whereas the band edges of BOC bend downwards due to electron accumulation. During light illumination, electrons from BOC and carbon polymers are excited from the VB to the CB. The interplay of the internal electric field, band bending, and Coulombic interactions accelerates the partial recombination of electrons (originating from the CB of BOC) and holes (originating from the VB of carbon polymers), while concurrently suppressing the partial recombination of electrons (arising from the CB of carbon polymers) and holes (arising from the VB of BOC). This dynamic carrier migration process at the heterojunction interface underscores the exceptional redox capabilities of the CN/BOC and CPDs/BOC photocatalysts and provides a potent driving force in their photocatalytic reactions.

The charge transfer mechanism is supported by the surface potential difference before and after irradiation measured by KPFM. In Fig. S3a, the surface photovoltage distribution of the 10 wt% CN/p-BOC composites is depicted under dark conditions, while Fig. S3b illustrates the distribution under visible light irradiation ($\lambda > 400$ nm). Fig. S3c delineates the surface potentials from position A to position B in the visual image. Following visible light exposure, the surface potential at position A (carbon-based polymer) decreased by approximately 20 mV, whereas at position B (BOC), it increased by around 16 mV. This positive shift of the BOC surface potential upon illumination indicates accumulation of positive photogenerated charge carrier, holes, on the BOC surface [9, 52]. Conversely, the reverse bias observed in the surface potential of the carbon-based polymer upon illumination indicates the accumulation of photoinduced electrons on its surface. These findings indicate that the electric field direction is from the carbon-based polymer toward BOC. Photogenerated electrons migrate from BOC to CN under visible light irradiation. To further confirm the charge transfer path, Ag and MnOx are photodeposited using AgCl and MnSO₄ as precursors on 10 wt% CN/BOC. Ag is distributed on CN of 10 wt% CN/BOC (Fig. 4f), while Mn is distributed on BOC of 10 wt% CN/BOC (Fig. 4g). Hence, the photogenerated electrons tend to accumulate on the carbon polymers to participate in reduction ($\text{Ag}^+ + \text{e}^- \rightarrow \text{Ag}$), while the photogenerated holes trigger oxidation in BOC ($\text{Mn}^{2+} + \text{x H}_2\text{O} + (2\text{x}-2) \text{h}^+ \rightarrow \text{MnO}_\text{x} + 2\text{x H}^+$). Both results strongly validate the charge transfer pathways of the carbon polymer/BOC S-scheme heterojunction, consistent with both theoretical calculations and XPS characterization results.

3.3. Photocatalytic properties

RhB is a synthetic organic dye known for its vibrant red color, commonly employed in industrial settings for the dyeing of paper and fabrics. Despite its widespread use, RhB poses significant risks to human health, manifesting in symptoms such as skin discoloration, internal organ staining, mild bruising of interstitial blood vessels in the brain, and breakage of heart muscle fibers [48]. On the other hand, TC, classified as an antibiotic, demonstrates efficacy against rickettsiae, trachoma virus, and gram-negative bacilli. While it exerts a bactericidal effect at high concentrations, its clinical use is hindered by notable side effects on the gastrointestinal tract, susceptibility to secondary infections, and adverse effects on bones and teeth, resulting in a decreased utilization rate and heightened environmental pollution [53]. Similarly,

CIP, another antibiotic, exhibits potent bactericidal and antibacterial properties but is associated with systemic damage, particularly allergic reactions, and heightened impacts on the nervous system and skin [54]. Therefore, the governance of RhB, TC and CIP is a pressing issue.

The photocatalytic properties are assessed by photodegradation experiments using the RhB, TC and CIP organic pollutant under visible light irradiation. As shown in Fig. 5a-f for RhB, TC, and CIP, minimal self-degradation is observed in the absence of photocatalysts. Both the individual p-BOC, CN and n-BOC monomers display suboptimal photocatalytic activity. The removal of RhB by p-BOC and CN after 120 min of visible light was about 72 % and 81 %, respectively, the removal of TC by p-BOC and CN after 100 min of visible light was 60 % and 71 %, respectively, and the removal of CIP by p-BOC and CN after 150 min of visible light was only 41 % and 56 %, respectively. Similarly, n-BOC exhibits lower degradation efficiency manifested by removal rates of 50% for RhB after 40 minutes, 68 % for TC after 75 minutes, and 57 % for CIP after 100 minutes. In contrast, all the composite materials have significantly improved degradation capabilities than the BOC monomers. Notably, the photocatalytic degradation performance of 10 wt% CN/p-BOC and 1 wt% CPDs/n-BOC stands out. 10 wt% CN/p-BOC shows removal rates of 97 % for RhB after visible light exposure for 120 minutes, 92 % for TC after 100 minutes, and 96 % for CIP after 150 minutes. In comparison, 1 wt% CPDs/n-BOC shows high degradation efficiency as exemplified by removal rates of 99 % for RhB after 40 minutes, 97 % for TC after 75 minutes, and 94 % for CIP after 100 minutes.

These results suggest that the photocatalytic degradation kinetics of RhB by p-BOC and n-BOC catalysts follow pseudo-first-order reactions, as illustrated in Fig. 5g and Fig. S4. The photocatalytic degradation kinetics of TC and CIP are represented by the following equation: $-\ln(C/C_0) = kt$, where k represents the rate constant, as depicted in Fig. 5h-i [55]. The rate constants for photocatalytic degradation of TC by p-BOC, n-BOC, 10 wt% CN/p-BOC, and 1 wt% CPDs/n-BOC are 0.00913, 0.01546, 0.02076, and 0.04327 min^{-1} , respectively. With regard to CIP, the rate constants of p-BOC, n-BOC, 10 wt% CN/p-BOC, and 1 wt% CPDs/n-BOC are 0.0058, 0.00716, 0.01665, and 0.02498 min^{-1} , respectively. Consequently, the rate constant for TC degradation by 1 wt % CPDs/n-BOC is 4.3 times greater than that of p-BOC and 2.8 times greater than that of n-BOC. Similarly, regarding CIP degradation, it is 4.3 times higher than that of p-BOC and 3.5 times higher than that of n-BOC. Notably, the photocatalytic degradation performance of 1 wt% CPDs/n-BOC surpassed that of 10 wt% CN/p-BOC, exhibiting improvements of 2.7, 2.1, and 1.50 times for RhB, TC, and CIP, respectively. Photocatalytic degradation of real urban sewage was carried out using the best performing 1 wt% CPDs/n-BOC. Actual municipal wastewater withdrawal locations are shown in Fig. S5a-b. Visible light-induced photocatalytic degradation was conducted with just one simple filtering of the sewage, and subsequent Total Organic Carbon (TOC) analysis revealed a nearly 70% reduction in TOC levels after two hours of photocatalytic degradation (Fig. S5c). This demonstrates the outstanding photocatalytic degradation capability of 1 wt% CPDs/n-BOC.

The stability of 10 wt% CN/p-BOC and 1 wt% CPDs/n-BOC is assessed by cycling experiments. The catalysts after the photocatalytic tests were washed and centrifuged three times using anhydrous ethanol and deionized water, respectively, before being dried and processed for use. To investigate whether the crystalline phase of the samples changed during the cyclic testing process. We chose the samples at 2, 4, 6, 8 and 10 cycles for XRD testing. After 10 cycles, the photocatalytic degradation performance of 10 wt% CN/p-BOC and 1 wt% CPDs/n-BOC shows only marginal reductions of 9 % and 7 %, respectively (Fig. S5a and d). Analysis by XRD (Fig. S5b and e) and TEM (Fig. S5c and f) of the collected photocatalysts after cycling reveals no significant alterations in the structure of 10 wt% CN/p-BOC and 1 wt% CPDs/n-BOC indicating the robust stability.

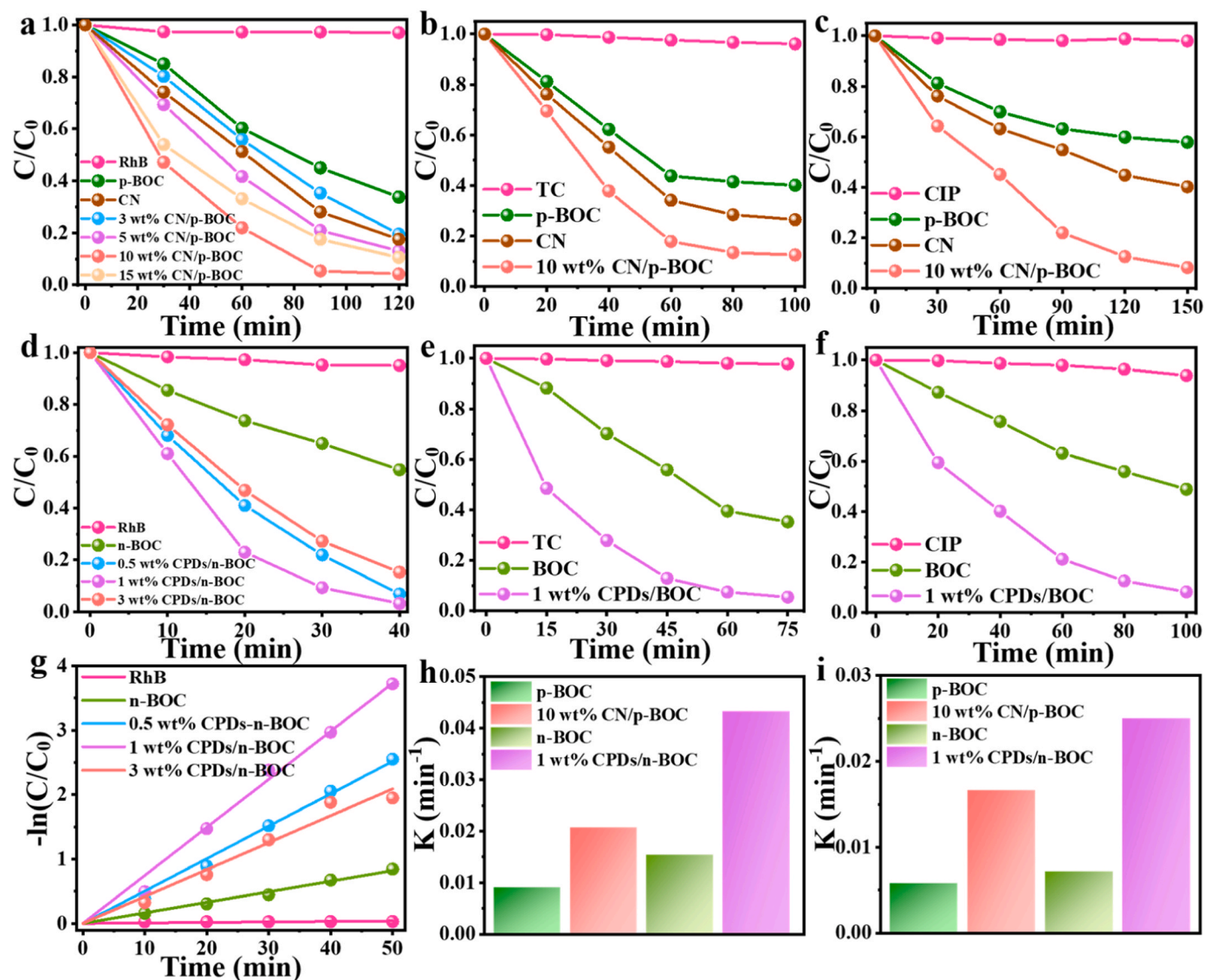


Fig. 5. Photocatalytic degradation under visible light irradiation of the CN/p-BOC samples for (a) RhB, (b) TC, and (c) CIP; Photocatalytic degradation under visible light exposure of the CPDs/n-BOC samples for (d) RhB, (e) TC, and (f) CIP; (g) Kinetics curves illustrating the degradation of RhB by the n-BOC samples; Kinetics curves of photocatalytic degradation of (h) TC and (i) CIP by the different samples.

3.4. Photocatalytic seawater purification

To evaluate the influence of various inorganic ions on the photocatalytic degradation of RhB, deionized water is replaced by an inorganic ion solution with a concentration of 1.0 mmol/L. Our aim is to understand how these inorganic ions affect the photocatalytic degradation of RhB. The experiments involve chloride salts such as NaCl, KCl, NH_4Cl , CaCl_2 , and MgCl_2 for 10 wt% CN/p-BOC and 1 wt% CPDs/n-BOC (Fig. 6a and d). Furthermore, the role of anions is investigated using sodium salts such as NaCl, Na_2SO_4 , NaBr, Na_2CO_3 , and NaHCO_3 (Fig. 6b and e). The experimental results indicate that these inorganic ions do not hinder the photocatalytic activity of 10 wt% CN/p-BOC and 1 wt% CPDs/n-BOC.

To determine the photocatalytic characteristics at different pH, HCl and NaOH are added. RhB exhibits enhanced degradation under acidic conditions, especially when the pH decreases from 13.0 to 1.0 (Fig. 6c and f) because RhB is a basic molecule that readily interacts with the catalyst by electrostatic adsorption and hydrogen bonding under acidic conditions [5]. However, an excessive concentration of OH^- in the solution can result in mutual repulsion between RhB and the catalyst due

to their negatively charged surfaces, subsequently affecting the adsorption of RhB.

To further assess the photocatalytic performance in the natural environment, degradation of RhB is monitored in seawater that has undergone only three rounds of filtration in a natural environment. It is evident that 10 wt% CN/p-BOC and 1 wt% CPDs/n-BOC exhibit no significant decrease in the degradation of RhB, TC, and CIP in seawater (Fig. 7a-f) due to the excellent ion interference resistance of 10 wt% CN/p-BOC and 1 wt% CPDs/n-BOC and minimal pH difference between seawater and deionized water. Photocatalytic degradation of real urban sewage was carried out using the best performing 1 wt% CPDs/n-BOC. Actual municipal wastewater withdrawal locations are shown in Fig. S6a-b. Visible light-induced photocatalytic degradation was conducted with just one simple filtering of the sewage, and subsequent Total Organic Carbon (TOC) analysis revealed a nearly 71 % reduction in TOC levels after six hours of photocatalytic degradation (Fig. S6c). This indicates that 1 wt% CPDs/n-BOC maintains excellent photocatalytic performance in various natural environments.

To harness the power of natural sunlight for seawater purification, a novel photocatalytic wastewater treatment apparatus was developed

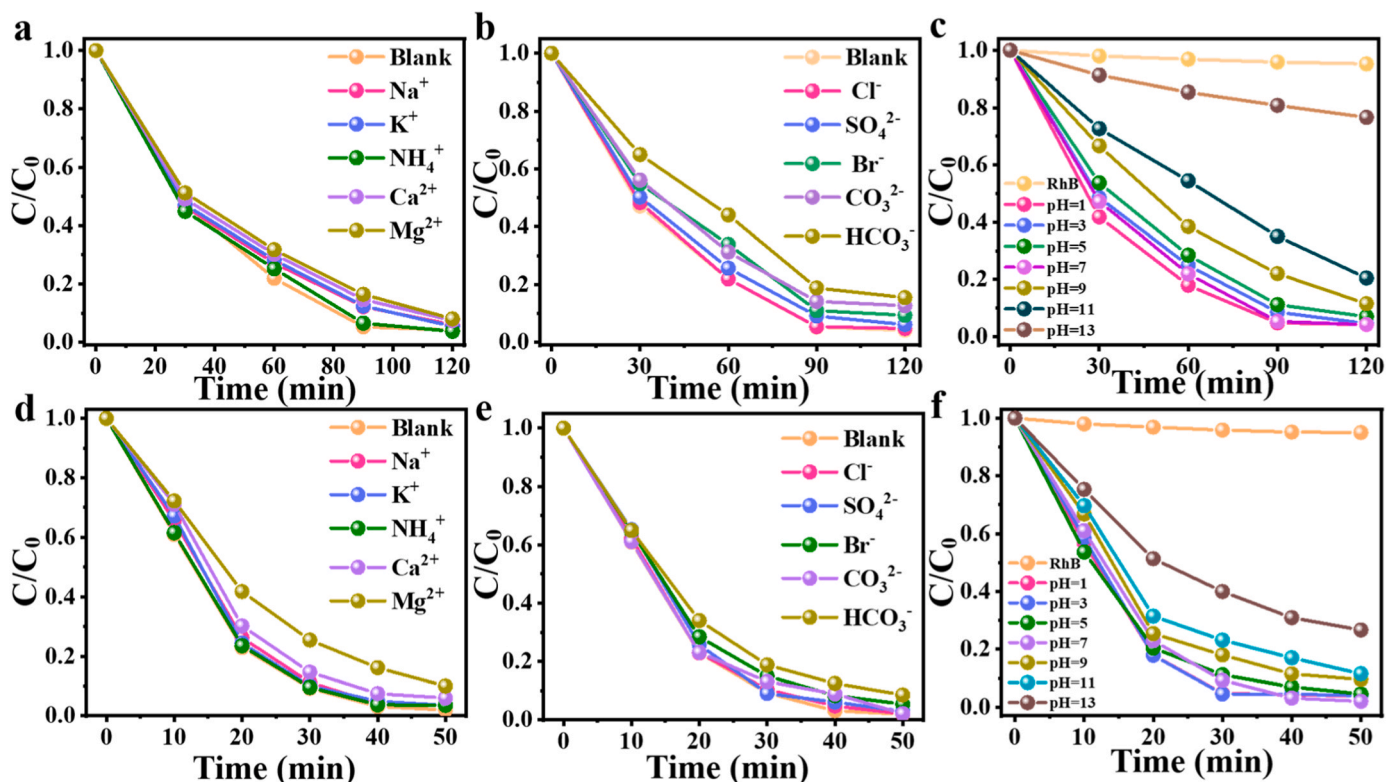


Fig. 6. (a) Effects of positive ions and (b) negative ions on photocatalytic degradation of RhB by 10 wt% CN/p-BOC; (c) Activity of 10 wt% CN/p-BOC in visible light degradation of RhB at different pH; (d) Effects of positive ions and (e) negative ions on photocatalytic degradation of RhB by 1 wt% CPDs/n-BOC; (f) Activity of 1 wt% CPDs/n-BOC in visible light degradation of RhB under different pH conditions.

(Fig. 7g and S7). This device relies on a readily prepared 1 wt% CPD/n-BOC photocatalyst, showcasing outstanding performance in the purification process. The apparatus is comprised of three main sections: photocatalytic reaction section, water storage compartment, and power-driven component, with detailed specifications illustrated in Fig. 7h-i. The photocatalytic reaction section is located on the uppermost level and consists of reaction surface and recirculation tank. The reaction surface is composed of a film layer containing 1 wt% CPDs/n-BOC photocatalytic material and naphthol. Positioned below is the water storage compartment, constructed from acrylic material, while the power-driven component consists of two water pumps. At the start of the experiment, a 20 L solution of 100 mg/L RhB seawater is introduced into the water storage compartment, and the photocatalytic reaction apparatus coated with 1 wt% CPDs/n-BOC is mounted on top. The power system is then activated to initiate water circulation. Photocatalytic degradation of 20 L of 100 mg/L RhB seawater is conducted under natural light conditions (Video. S1) and RhB is decomposed completely after 5 hours (Fig. 7j). The natural light-driven automated photocatalytic wastewater treatment device used in the experiment has a simple structure and is easy to operate. Compared with traditional photocatalytic devices, this system operating on natural light offers advantages such as energy saving, environmental protection, and sustainability.

Supplementary material related to this article can be found online at [doi:10.1016/j.apcatb.2024.124050](https://doi.org/10.1016/j.apcatb.2024.124050).

3.5. Degradation pathways of pollutants

In order to elucidate the mechanism of the photocatalytic degradation of RhB, TC, and CIP, experiments are performed at various time intervals during visible light exposure and the products are analyzed by LC-MS (Fig. S8). During extended light exposure, a gradual decrease in the peak intensity is observed from the RhB molecules ($m/z = 443$), TC

molecules ($m/z = 445$), and CIP molecules ($m/z = 332$), while the smaller m/z compounds show a temporary increase in the intensities followed by a decrease. These findings suggest progressive degradation of organic pollutants into smaller molecular byproducts, which are further mineralized during continuous light exposure. Fig. S9a-b present the mass spectra of molecular intermediates generated during the photocatalytic degradation of RhB. As shown in Fig. 8a, based on the m/z values of these intermediates and structural characteristics of RhB, a degradation and mineralization pathway involving N-demethylation, chromophore cleavage, ring opening, and eventual mineralization is postulated. Specifically, the m/z values of 443, 415, 387, 359, and 331 correspond to RhB, N, N-ethyl-N'-ethyl rhodamine, N-ethyl-N'-ethyl rhodamine, N-ethyl rhodamine, and rhodamine, respectively. These transformations ultimately lead to the formation of phthalic anhydride, oxalic acid, and eventual mineralization into CO_2 and H_2O . As for the LC-MS results for TC (Fig. S9c-d), multiple intermediates are identified to delineate the three degradation pathways shown in Fig. 8b. In the presence of the reactive species, the first pathway involves the removal of N-dimethyl groups, ring opening, formation of $C_{17}H_{17}NO_6$ ($m/z = 311$), and subsequent oxidation produces $C_{10}H_{10}O_4$ ($m/z = 194$). In the alternative degradation pathway, initial removal of methyl and hydroxyl groups prompts ring opening and creation of $C_{18}O_{20}N_2O_8$ ($m/z = 392$), which undergoes subsequent ring opening to yield $C_{15}O_{18}N_2O_6$ ($m/z = 322$). The ring opening and oxidation processes generate small alcohols, acids, and amines, which ultimately mineralize into CO_2 , H_2O , NO_3^- , and NH_4^+ .

To obtain a better understanding of the transformation mechanism of CIP in photocatalysis, LC-MS is conducted (Fig. S9e-f). Fig. 8c describes the pathway of CIP photocatalysis by 1 wt% CPDs/n-BOC. The 6 N position in the CIPs piperazine ring emerges as the most susceptible one to influence the reactive species. However, due to steric hindrance and saturation, the 6 N site is reluctant to accept free radicals. Concurrently, the tertiary amine possesses potent electron-withdrawing properties,

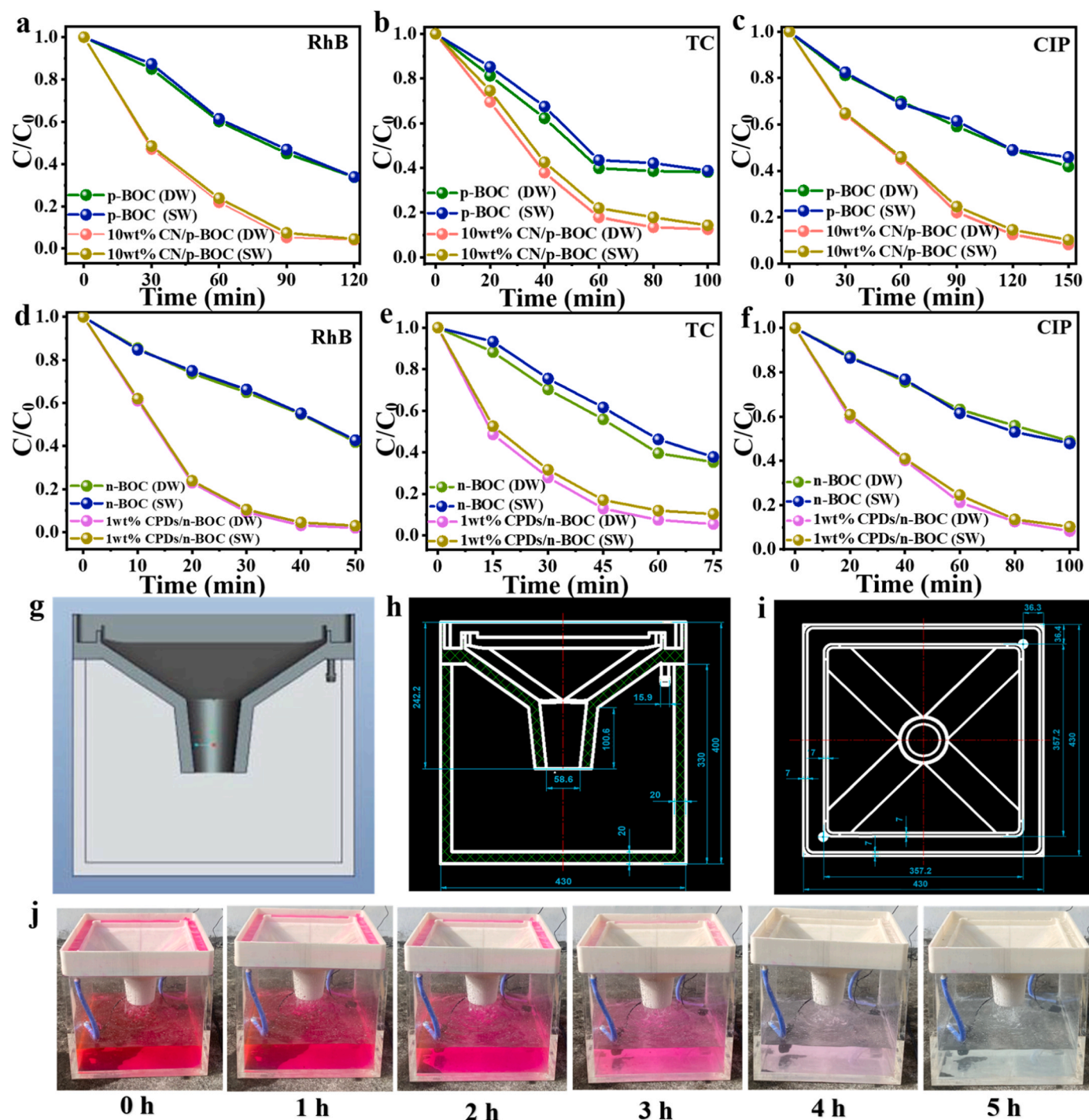


Fig. 7. Photocatalytic degradation of (a) RhB, (b) TC, and (c) CIP by 10 wt% CN/p-BOC in seawater and deionized water; Photocatalytic degradation of (d) RhB, (e) TC, and (f) CIP by 1 wt% CPDs/n-BOC in seawater and deionized water; (g) Design drawing, (h-i) specification drawings and (j) results of work for natural light-driven automated photocatalytic wastewater treatment device.

rendering the α -carbon on the piperazine ring to be the next most accessible target for attack by neighboring reactive species. The reactive species initiate an attack on CIP, leading to the formation of an endoperoxide, which subsequently decomposes to produce an acetaldehyde moiety and gives rise to the product C1 ($m/z = 362$). C1 is susceptible to attack by H^+ , leading to hydrolysis and generation of C2 ($m/z = 334$) together with its isomer CA2 ($m/z = 342$). Aldehyde decomposition results in the formation of C3 ($m/z = 274$) and CA3 ($m/z = 306$). C3 further undergoes oxidation to yield C4 ($m/z = 245$). Alternatively, CIP may initially shed a carboxyl group to produce CB1 ($m/z = 288$), which

is vulnerable to attack by reactive species, resulting in the removal of a cyclopropane ring and formation of CB2 ($m/z = 248$). Ultimately, the products stemming from all the pathways undergo photodegradation to form smaller oxygen-containing compounds, culminating in their mineralization into water and carbon dioxide.

Building upon the aforementioned findings and existing literature, it has been observed that predominant transformation reactions in antibiotic processes often occur on substituent groups with minimal disruption to their core skeleton. This tendency frequently results in transformation products with heightened biological activity [56]. In

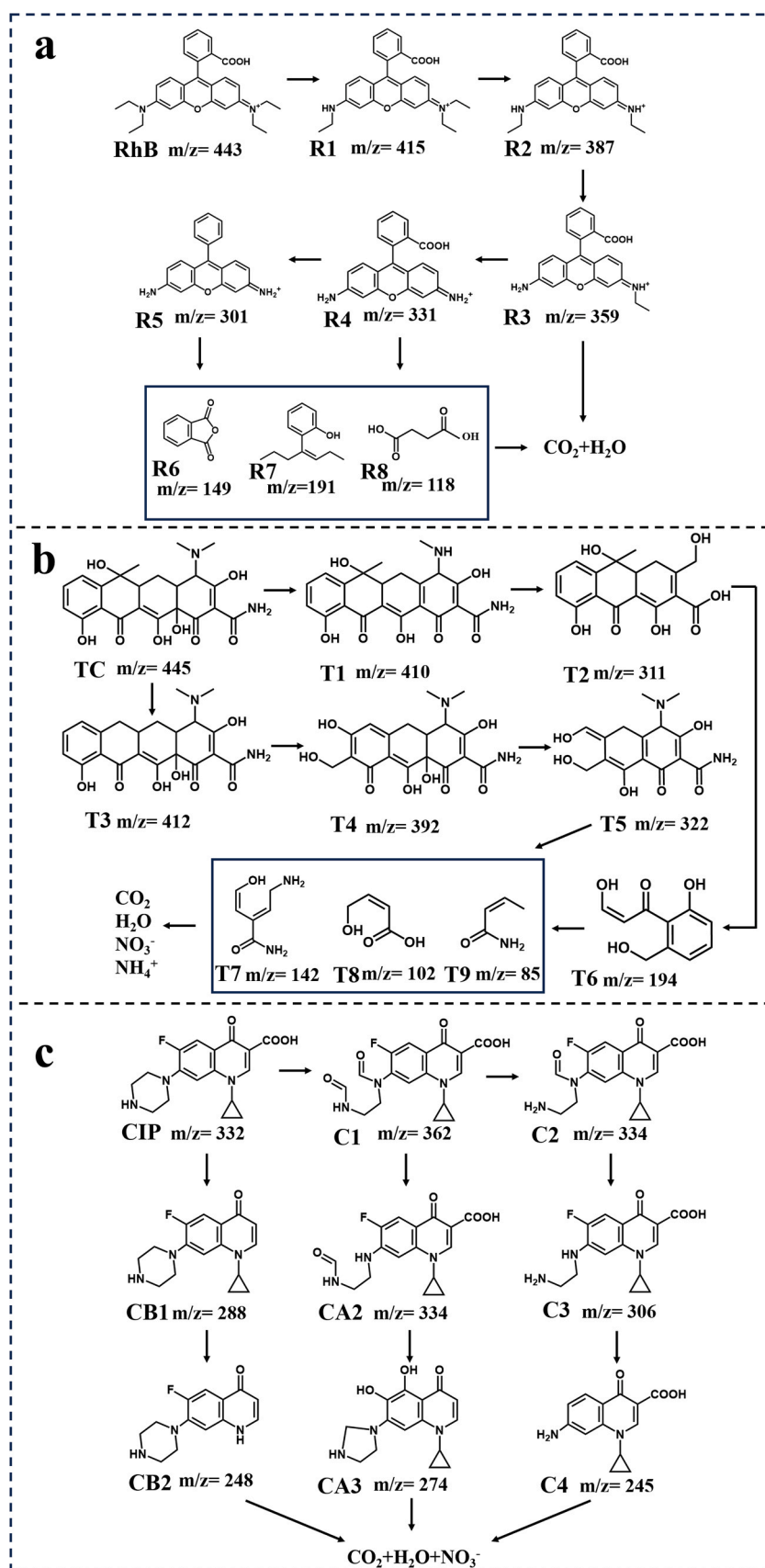


Fig. 8. Possible degradation pathways of (a) RhB, (b) TC, and (c) CIP by 1 wt% CPDs/n-BOC.

light of this, the ecotoxicity of RhB, CIP, and TC, as well as their transformation products, was further assessed across a diverse spectrum of species using the Toxicity Estimation Software Tool model. The toxicity levels were categorized into four classes according to the Globally Harmonized System of Classification and Labelling of Chemicals (refer to Table S3). As illustrated in Fig. 9a-b, the overall toxicity of the transformation products demonstrated effective suppression, although a select few exhibited elevated toxicity levels, posing potential environmental risks. Notably, most of these toxic intermediates are characterized by their instability, and hydroxyl radicals play a pivotal role in neutralizing these unstable compounds [57]. Consequently, these compounds undergo further degradation into carbon dioxide and water. In accordance with the outlined reaction mechanism, the transformation products contribute to the reduction of pollutant toxicity, illustrating a promising avenue for mitigating environmental risks.

To further demonstrate the reduced toxicity of contaminants, employed the products resulting from photocatalytic degradation to cultivate mung beans for toxicity assessment (Fig. 9c-f). Initially, the mung beans underwent a 5-hour soaking period in deionized water. Subsequently, the mung beans were segregated into seven groups, each comprising 50 mung beans, and were positioned in a well-ventilated area shielded from light. Every 12 hours for a duration of 10 minutes, the mung beans in each group were sequentially immersed in deionized water, RhB solution (R), RhB degradation product (Rw), TC solution (T), TC degradation product (Tw), CIP solution (C), and CIP degradation product (Cw). After each immersion, the mung beans were removed and placed in a ventilated area shielded from light (refer to Fig. S10 for the growth stages of mung beans). The average lengths of bean sprouts irrigated with the degradation products measured 10.2 cm, 9.5 cm, and 9.3 cm, respectively. These lengths were closely comparable to those of mung beans cultivated in deionized water (with an average length of 11.1 cm). Notably, the germination of mung beans in the untreated contaminant solution was markedly low and sluggish. This observation underscores that the toxicity of the degradation products, post-treatment with the composite catalyst, is significantly lower than that of the original pollutants.

3.6. Optical, electronic, and mechanistic assessment

EIS is employed to investigate the resistance during charge transfer and a smaller Nyquist arc diameter indicates a lower resistance. Fig. 10a-b show that 10 wt% CN/p-BOC and 1 wt% CPDs/n-BOC have Nyquist diameters smaller than that of the monomeric BOC. This observation confirms the superior efficiency of charge transfer in the composite materials [58]. The transient photocurrent response spectra are depicted in Fig. 10c-d. The composite materials, 10 wt% CN/p-BOC, and 1 wt% CPDs/n-BOC show better and more stable photocurrent response than the monomers for six on-off cycles due to excellent electron migration [59]. The steady-state PL spectra are acquired to probe the separation and recombination of photoexcited electrons and holes [60]. Fluorescence from the composite materials is weaker than that from the monomeric BOC (Fig. 10e-f) due to suppression of charge recombination. It is confirmed by the time-resolved photoluminescence spectra (Fig. 10g-h), which reveal improved separation efficiency of electrons and holes [61]. The surface photovoltage arising from surface photoelectrochemical reactions not only facilitates electron migration, but also contributes to catalyst reduction to ultimately enhance the photocatalytic activity. A high carrier separation efficiency enables more efficient utilization of the incident light and in turn, produces larger surface photocurrents and surface photovoltage [62]. The experimental results indicate a stronger surface photovoltage response from the composite materials (Fig. 10i). In summary, superior light-induced carrier transfer and separation efficiency is observed from 1 wt% CPDs/n-BOC.

The electrochemically active specific surface area (ECSA) was determined based on the double layer capacitance (Cdl) results obtained from cyclic voltammetry (CV) [63]. The potential versus current density curves at varying scan rates presented in Fig. S11 were subjected to fitting analysis, as illustrated in Fig. S12. The fitted curves revealed distinct slopes for p-BOC ($0.0124 \text{ mF}\cdot\text{cm}^{-2}$), n-BOC ($0.01496 \text{ mF}\cdot\text{cm}^{-2}$), CN ($0.01421 \text{ mF}\cdot\text{cm}^{-2}$), CPDs ($0.01609 \text{ mF}\cdot\text{cm}^{-2}$), 10 wt% CN/p-BOC ($0.01643 \text{ mF}\cdot\text{cm}^{-2}$) and 1 wt% CPDs/n-BOC ($0.02158 \text{ mF}\cdot\text{cm}^{-2}$), respectively. Notably, both composite materials exhibited higher

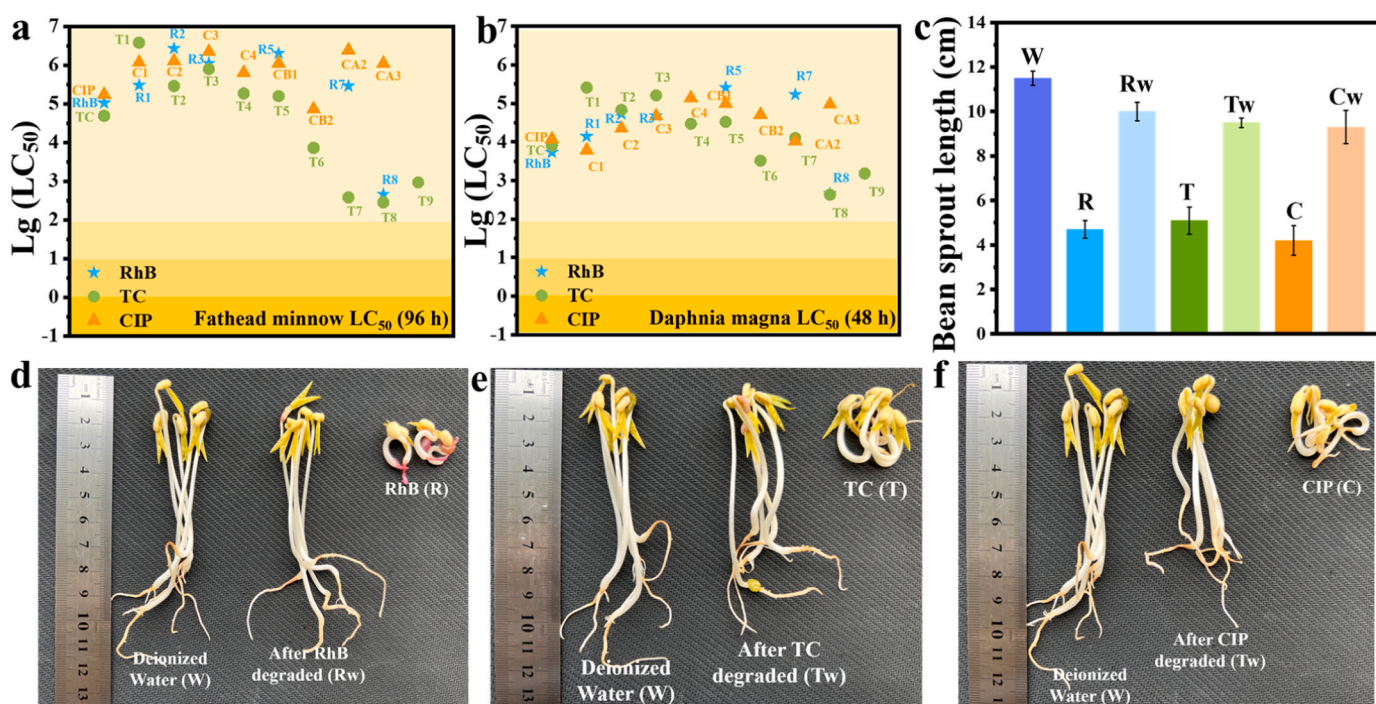


Fig. 9. (a-b) Predicting the toxicity of pollutants and their transformation products. (c) Mean length and (d-f) growing situation of mung bean seeds before and after photocatalytic degradation in deionized water and solution.

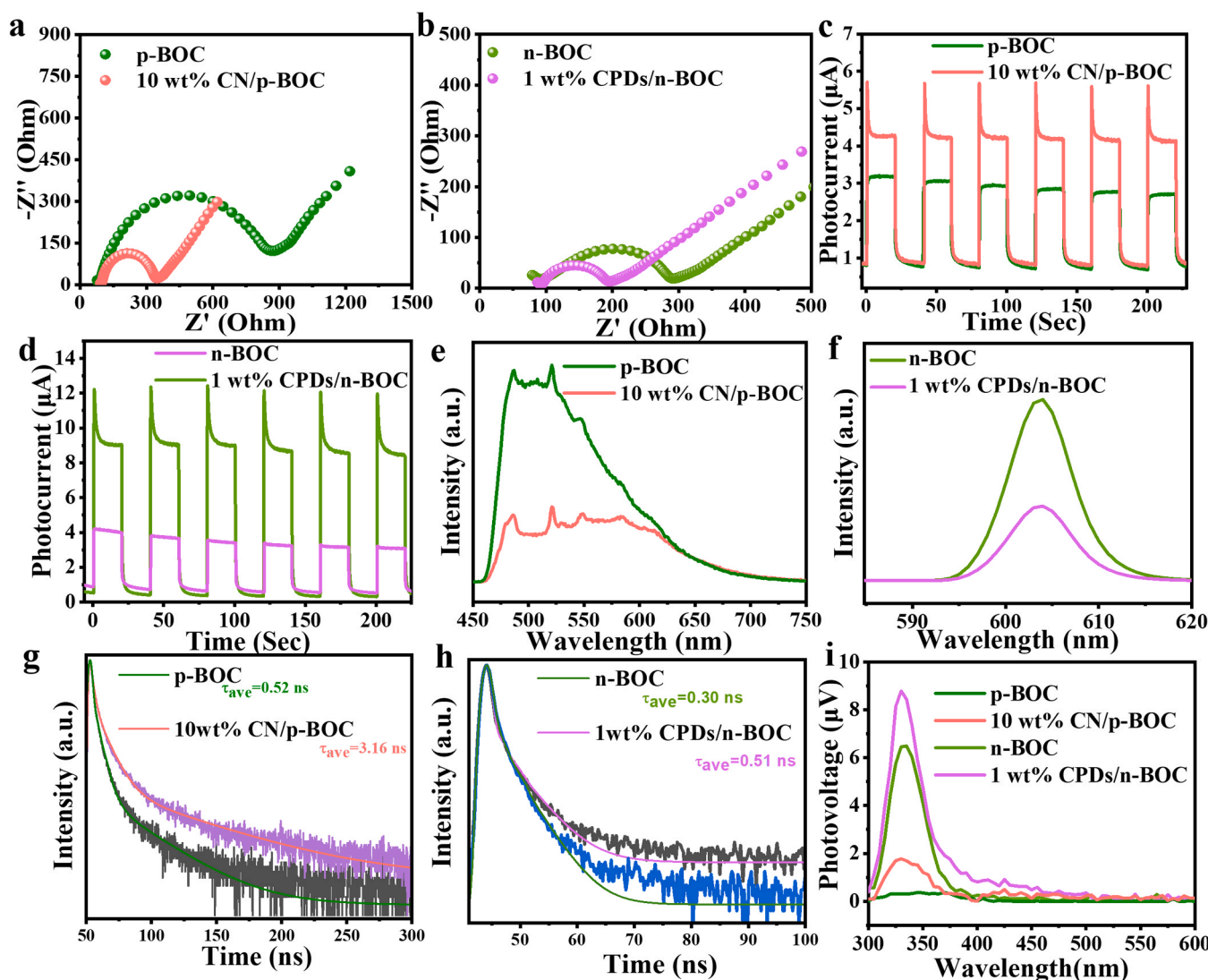


Fig. 10. (a–b) Electrochemical impedance diagrams, (c–d) Transient photocurrent response spectra, (e–f) PL spectra, (g–h) Transient fluorescence spectrogram, and (i) Surface photovoltage spectra of the photocatalysts.

electrochemical activity compared to their individual monomers. Remarkably, 1 wt% CPDs/n-BOC demonstrated the largest electrochemically active specific surface area among all the materials evaluated. This signifies a higher abundance of active sites for photocatalytic degradation, indicating its superior potential for catalytic performance.

To identify the active species involved in the degradation process, free radical trapping experiments and ESR are conducted. The former experiments are performed with 10 wt% CN/p-BOC and the results are shown in Fig. 11a. IPA serves as the $\cdot\text{OH}$ scavenger, ammonium oxalate AO and triethanolamine TEA act as the hole scavengers, and N_2 serves as the $\cdot\text{O}_2$ inhibitor [64]. The scavengers have a significant impact on the degradation efficiency of RhB, indicating the crucial roles of $\cdot\text{O}_2$, holes, and $\cdot\text{OH}$ in the degradation process. ESR is carried out to confirm the presence of active oxygen species (Fig. 11b–c). Under dark conditions, there are no signals of DMPO- $\cdot\text{O}_2$ and DMPO- $\cdot\text{OH}$ for both materials, indicating no active oxygen generation [65]. However, under light illumination, the materials exhibit a signal for DMPO- $\cdot\text{O}_2$, and 10 wt% CN/p-BOC shows a stronger signal than p-BOC, suggesting more $\cdot\text{O}_2$ generation in the presence of 10 wt% CN/p-BOC. The DMPO- $\cdot\text{OH}$ signal is observed from 10 wt% CN/p-BOC but not from BOC due to the high $\cdot\text{O}_2$ concentration, leading to the partial conversion of $\cdot\text{O}_2$ to $\cdot\text{OH}$. The ESR and free radical trapping results are consistent.

As shown in Fig. 11d, the addition of TEA, nitrogen, and AO inhibits

the activity of 1 wt% CPDs/n-BOC, and hence, h^+ and $\cdot\text{O}_2$ are the primary active species in photocatalytic degradation. However, the addition of IPA has a minimal impact on the RhB photodegradation activity by 1 wt% CPDs/n-BOC, suggesting a minor role of $\cdot\text{OH}$. Additionally, ESR does not reveal peaks for $\cdot\text{O}_2$ and $\cdot\text{OH}$ for both n-BOC and 1 wt% CPDs/n-BOC under dark conditions. However, after visible light exposure for 10 minutes, both n-BOC and 1 wt% CPDs/n-BOC show peaks for DMPO- $\cdot\text{O}_2$ but no DMPO- $\cdot\text{OH}$ peaks (Fig. 10e–f). The signal intensity of 1 wt% CPDs/n-BOC is stronger than that of the monomer, indicating that the composite materials produce a greater quantity of active species in the photocatalytic reaction.

The mechanism for the photocatalytic degradation of organic pollutants by the carbon-based polymer/BOC S-scheme heterojunction photocatalyst is postulated according to the spatial arrangement of VB, CB, and active species, as illustrated in Fig. 12. When BOC comes into close contact with the carbon-based polymer, electrons in the carbon polymers migrate spontaneously to BOC at the interface to balance the Fermi level. Consequently, the carbon-based polymer loses electrons and carries a positive charge, while BOC gains electrons and carries a negative charge, thereby creating a built-in electric field across the interface. At the same time, the band edge of the carbon polymer bends upward due to electron loss, while the band edge of BOC bends downward because of electron accumulation. Under light illumination,

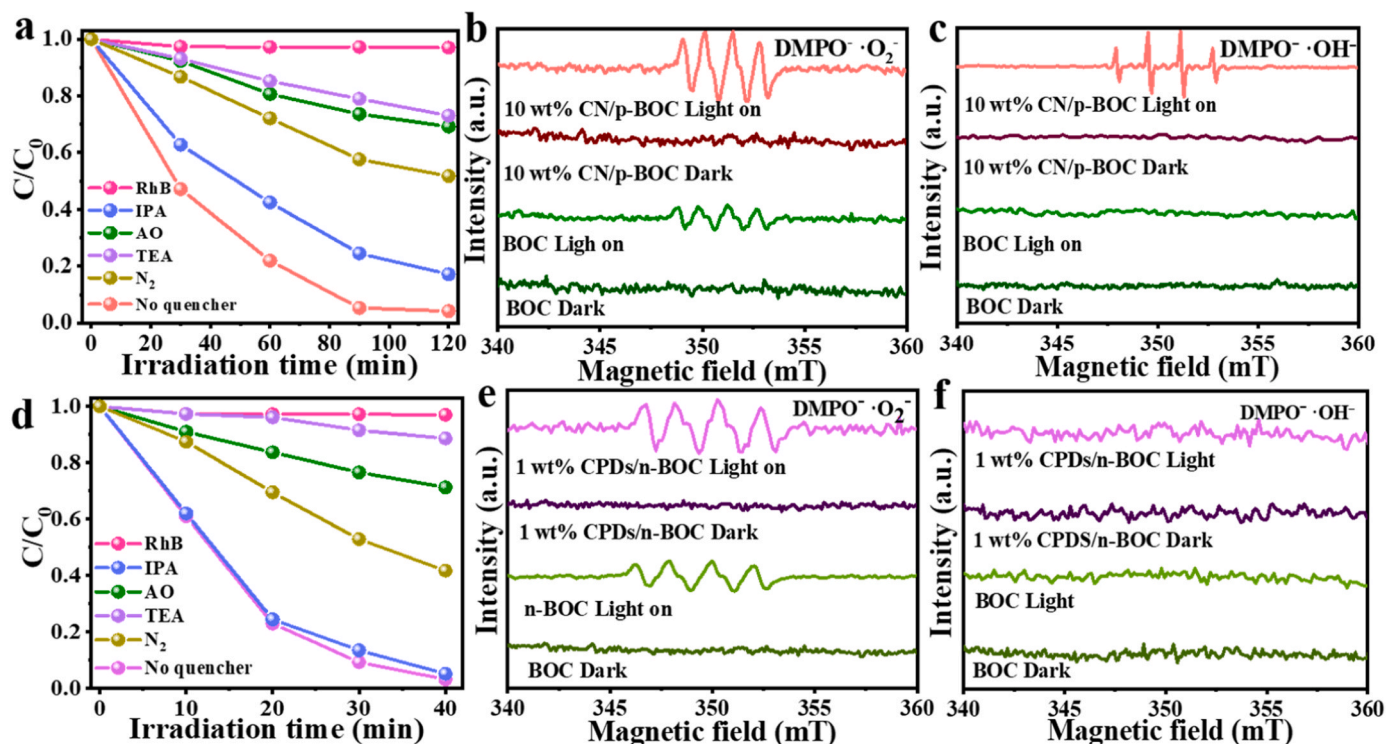


Fig. 11. (a) Photocatalytic degradation of RhB by 10 wt% CN/p-BOC under visible light illumination in the active substance capture experiments; ESR profiles: (b) $DMPO \cdot O_2^-$ and (c) $DMPO \cdot OH^-$; (d) Photocatalytic degradation of RhB by 1 wt% CPDs/n-BOC under visible light irradiation in the active substance capture experiments; ESR profiles: (e) $DMPO \cdot O_2^-$ and (f) $DMPO \cdot OH^-$.

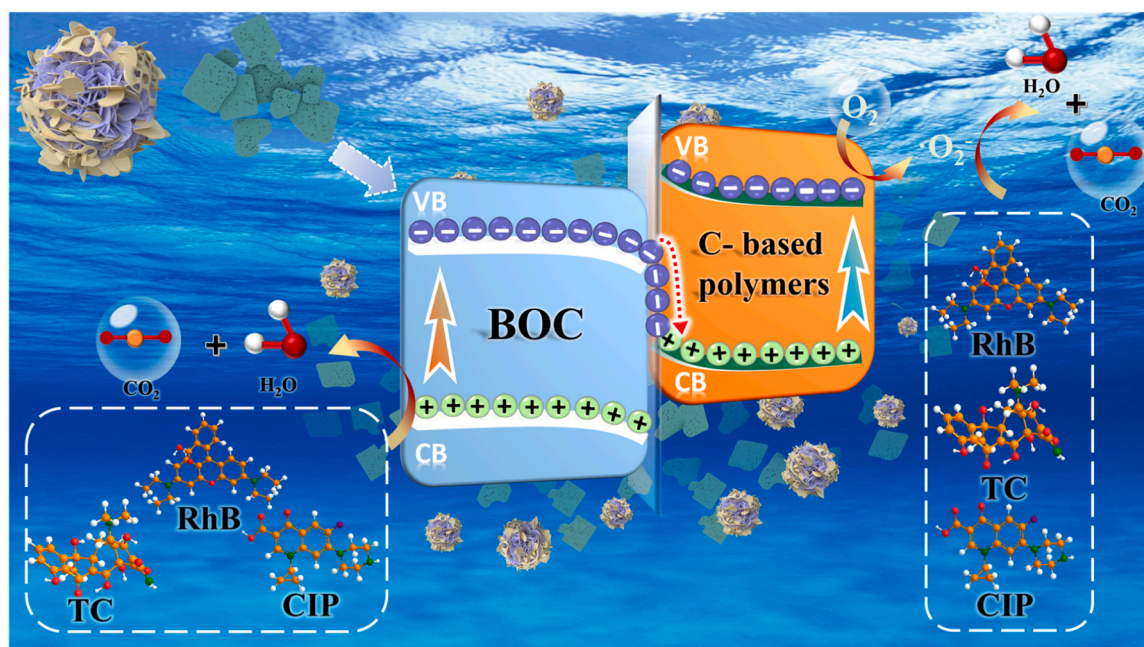


Fig. 12. Photocatalytic mechanism of carbon-based polymer/BOC.

electrons from both BOC and the carbon-based polymer are excited from the VB to CB. The built-in electric field, band edge bending, and Coulomb interactions accelerate the recombination of electrons (from the CB of BOC) and holes (from the VB of carbon polymers), thus impeding the recombination of electrons and holes in the respective semiconductor materials. Electrons in the valence band of carbon polymers and holes in the conduction band of BOC are retained. The

conduction band position of the carbon-based polymer is more negative thereby facilitating the conversion of oxygen molecules to $\cdot O_2^-$, while BOC possesses a higher valence band position than the carbon-based polymer but not exceeding the oxidation potential of $\cdot OH$. Consequently, holes in BOC cannot convert OH^- to $\cdot OH$, but can directly oxidize organic pollutants. Ultimately, h^+ and $\cdot O_2^-$ collaboratively transform organic pollutants into end products such as CO_2 and H_2O . In

conclusion, the S-scheme heterojunction of carbon-based polymer/BOC effectively segregates photogenerated electrons and holes while preserving the maximum redox capacity of the materials.

4. Conclusion

The carbon-based polymer/BOC S-scheme heterojunction is designed and fabricated. Enhancement of visible light absorption and redox properties is achieved by strategically optimizing the overall structure through a multi-dimensional construction approach. XPS, KPFM, photodeposition experiments, and theoretical calculations reveal the transfer of photoexcited electrons from BOC to the carbon-based polymer by the S-scheme mechanism. This strategy not only facilitates the separation of photogenerated carriers, but also preserves the potent oxidation and integrity of the reduction centers in the materials. The best-performing 1 wt% CPDs/n-BOC catalyst exhibits a remarkable improvement in the degradation of RhB, TC, and CIP compared to the BOC monomer, as exemplified by enhancements of 7.6, 4.7, and 4.3 times, respectively. Furthermore, it has excellent cycling stability as manifested by only 7 % decrease after 10 cycles. The degradation pathways for RhB, TC, and CIP are elucidated by LC-MS. Since the 1 wt% CPDs/n-BOC catalyst is easy to prepare in large quantities and has excellent properties, a natural light-driven wastewater treatment system is constructed based on this catalyst. Our results reveal the high potential of the technique and materials for high-performance photocatalysis under real conditions.

CRediT authorship contribution statement

Shihao Jia: Conceptualization, Data curation, Investigation, Writing – original draft. **Huimin Han:** Data curation, Investigation. **Bin Wang:** Conceptualization, Resources, Writing – review & editing, Supervision. **Jinyuan Liu:** Data curation, Investigation. **Qi Tang:** Data curation, Investigation. **Gaopeng Liu:** Data curation, Investigation. **Qingdong Ruan:** Investigation, Writing – original draft. **Xingwang Zhu:** Investigation, Resources, Writing – review & editing, Supervision. **Huaming Li:** Resources, Supervision. **Chongtai Wang:** Resources, Supervision. **Paul K. Chu:** Resources, Writing – review & editing, Supervision. **Yingjie Hua:** Conceptualization, Resources, Writing – review & editing, Supervision.

Declaration of Competing Interest

There are no conflicts of interest

Data Availability

Data will be made available on request.

Acknowledgments

This work was financially supported by the National Natural Science Foundation of China (No. 22108106, 22008095, 22308300), Natural Science Foundation of Jiangsu Province (No. BK20220598), China Postdoctoral Science Foundation (No. 2020M680065, 2022M721380), Hong Kong Scholar Program (No. XJ2021021), Key Laboratory of Electrochemical Energy Storage and Energy Conversion of Hainan Province (No. KFKT2021006), Grants for the Innovation Center of Academician Sun Shigang's Team in Hainan Province and Hainan Provincial Science and Technology Program (No. SQKY2022-0041), and City University of Hong Kong Donation Research Grant (DON-RMG No. 9229021).

Appendix A. Supporting information

Supplementary data associated with this article can be found in the

online version at [doi:10.1016/j.apcatb.2024.124050](https://doi.org/10.1016/j.apcatb.2024.124050).

References

- [1] T. Suzuki, T. Hidaka, Y. Kumagai, M. Yamamoto, Environmental pollutants and the immune response, *Nat. Immunol.* 211 (2020) 1486–1495, <https://doi.org/10.1038/s41590-020-0802-6>.
- [2] L. Cai, Z. Jiang, J. Shanguan, T. Qing, P. Zhang, B. Feng, Applications of carbon dots in environmental pollution control: A review, *Chem. Eng. J.* 406 (2021) 126848, <https://doi.org/10.1016/j.cej.2020.126848>.
- [3] K. Guo, C. Yu, B. Gao, B. Liu, Z. Wang, Y. Wang, Q. Yue, Y. Gao, Intrinsic mechanism for the removal of antibiotic pollution by a dual coagulation process from the perspective of the interaction between NOM and antibiotic, *Water Res.* 244 (2023) 120483, <https://doi.org/10.1016/j.watres.2023.120483>.
- [4] J. Sun, L. Liu, F. Yang, A visible-light-driven photocatalytic fuel cell/peroxymonosulfate (PFC/PMS) system using blue TiO₂ nanotube arrays (TNA) anode and Cu-Co-WO₃ cathode for enhanced oxidation of organic pollutant and ammonium nitrogen in real seawater, *Appl. Catal. B* 308 (2022) 121215, <https://doi.org/10.1016/j.apcatb.2022.121215>.
- [5] S. Jia, B. Wang, J. Liu, G. Liu, X. Zhu, H. Han, Q. Tang, Y. Hua, C. Wang, H. Li, Morphology normalization of peony flower-like Bi₂O₂CO₃ boosts photocatalytic seawater purification, *Colloids Surf. A Physicochem. Eng. Asp.* 653 (2022) 129915, <https://doi.org/10.1016/j.colsurfa.2022.129915>.
- [6] J.E. Elliott, K.H. Elliott, Tracking marine pollution (<https://www.science.org/doi/>), *Science* 340 (2013) 556–558, <https://doi.org/10.1126/science.1235197>.
- [7] L. Xu, P.K. Wong, Z. Jiang, J.C. Yu, Iodide-mediated selective photocatalytic treatment of phenolic pollutants, *Appl. Catal. B* 338 (2023) 123080, <https://doi.org/10.1016/j.apcatb.2023.123080>.
- [8] Q. Lu, L. Yang, P.C. Ayala, Y. Li, X. Zhang, M.G. El-Dinb, Enhanced photocatalytic degradation of organic contaminants in water by highly tunable surface microlenses, *Chem. Eng. J.* 463 (2023) 142345, <https://doi.org/10.1016/j.cej.2023.142345>.
- [9] Y. You, S. Chen, J. Zhao, J. Lin, D. Wen, P. Sha, L. Li, D. Bu, S. Huang, Rational Design of S-Scheme Heterojunction toward Efficient Photocatalytic Cellulose Reforming for H₂ and Formic Acid in Pure Water, *Adv. Mater.* 36 (4) (2024) 2307962, <https://doi.org/10.1002/adma.202307962>.
- [10] J. Qiu, K. Meng, Y. Zhang, B. Cheng, J. Zhang, L. Wang, J. Yu, COF/In₂S₃ S-scheme photocatalyst with enhanced light absorption and H₂O₂-production activity and fs-TA investigation, *Adv. Mater.* (2024) 2400288, <https://doi.org/10.1002/adma.202400288>.
- [11] Y. Xia, H. Yang, W. Ho, B. Zhu, J. Yu, Promoting the photocatalytic NO oxidation activity of hierarchical porous g-C₃N₄ by introduction of nitrogen vacancies and charge channels, *Appl. Catal. B* 344 (2024) 123604, <https://doi.org/10.1016/j.apcatb.2023.123604>.
- [12] B. Zhu, J. Sun, Y. Zhao, L. Zhang, J. Yu, Construction of 2D S-Scheme Heterojunction Photocatalyst, *Adv. Mater.* (2023) 2310600, <https://doi.org/10.1002/adma.202310600>.
- [13] P. Kuang, Z. Ni, B. Zhu, Y. Lin, J. Yu, Modulating the d-band center enables ultrafine Pt₃Fe alloy nanoparticles for pH-universal hydrogen evolution reaction, *Adv. Mater.* 35.41 (2023) 2303030, <https://doi.org/10.1002/adma.202303030>.
- [14] Z. Wang, X. Yue, Q. Xiang, MOFs-based S-scheme heterojunction photocatalysts, *Coord. Chem. Rev.* 504 (2024) 215674, <https://doi.org/10.1016/j.ccr.2024.215674>.
- [15] X. Yue, L. Cheng, J. Fan, Q. Xiang, 2D/2D BiVO₄/CsPbBr₃ S-scheme heterojunction for photocatalytic CO₂ reduction: insights into structure regulation and Fermi level modulation, *Appl. Catal. B Environ.* 304 (2022) 120979, <https://doi.org/10.1016/j.apcatb.2021.120979>.
- [16] L. Zhang, J. Zhang, H. Yu, J. Yu, Emerging S-scheme photocatalyst, *Adv. Mater.* 34 (2022) 2107668, <https://doi.org/10.1002/adma.202107668>.
- [17] X. Ruan, C. Huang, H. Cheng, Z. Zhang, Y. Cui, Z. Li, T. Xie, K. Ba, H. Zhang, L. Zhang, X. Zhao, J. Leng, S. Jin, W. Zhang, W. Zheng, S.K. Ravi, Z. Jiang, X. Cui, J. Yu, A twin S-scheme artificial photosynthetic system with self-assembled heterojunctions yields superior photocatalytic hydrogen evolution rate, *Adv. Mater.* 35 (2023) 2209141, <https://doi.org/10.1002/adma.202209141>.
- [18] K. Zhang, Y. Zhang, D. Zhang, C. Liu, X. Zhou, H. Yang, J. Qu, D. He, Efficient photocatalytic water disinfection by a novel BP/BiOBr S-scheme heterojunction photocatalyst, *Chem. Eng. J.* 468 (2023) 143581, <https://doi.org/10.1016/j.cej.2023.143581>.
- [19] M. Dai, H. Yu, W. Chen, K. Qu, D. Zhai, C. Liu, S. Zhao, S. Wang, Z. He, Boosting photocatalytic activity of CdLa₂S₄/ZnIn₂S₄ S-scheme heterojunctions with spatial separation of photoexcited carriers, *Chem. Eng. J.* 470 (2023) 144240, <https://doi.org/10.1016/j.cej.2023.144240>.
- [20] C. Zhang, M. Jia, Z. Xu, W. Xiong, Z. Yang, J. Cao, H. Peng, H. Xu, Y. Xiang, Y. Jing, Constructing 2D/2D N-ZnO/g-C₃N₄ S-scheme heterojunction: efficient photocatalytic performance for norfloxacin degradation, *Chem. Eng. J.* 430 (2022) 132652, <https://doi.org/10.1016/j.cej.2021.132652>.
- [21] Y. Zhao, X. Liang, Y. Wang, H. Shi, E. Liu, J. Fan, X. Hu, Degradation and removal of Ceftriaxone sodium in aquatic environment with Bi₂WO₆/g-C₃N₄ photocatalyst, *J. Colloid Interface Sci.* 523 (2018) 7–17, <https://doi.org/10.1016/j.jcis.2018.03.078>.
- [22] F. Li, G. Zhu, J. Jiang, L. Yang, F. Deng, Arramel, X. Li, A review of updated S-scheme heterojunction photocatalysts, *J. Mater. Sci. Technol.* 177 (2024) 142–180, <https://doi.org/10.1016/j.jmst.2023.08.038>.
- [23] X. Zu, Y. Zhao, X. Li, R. Chen, W. Shao, Z. Wang, J. Hu, J. Zhu, Y. Pan, Y. Sun, Y. Xie, Ultrastable and efficient visible-light-driven CO₂ reduction triggered by

- regenerative oxygen-vacancies in $\text{Bi}_2\text{O}_2\text{CO}_3$ nanosheets, *Angew. Chem. Int. Ed.* 60 (2021) 13840–13846, <https://doi.org/10.1002/anie.202101894>.
- [24] Y. Zhao, W. Liu, W. Shao, L. Li, M. Zuo, J. Hu, J. Zhu, H. Wang, X. Zhang, Elemental doping inhibits surface-state-mediated charge carrier trapping for promoting photocatalytic selective oxidation, *J. Mater. Chem. A* 11 (2023) 3594–3598, <https://doi.org/10.1039/D2TA09702H>.
- [25] J. Li, C. He, N. Xu, K. Wu, Z. Huang, X. Zhao, J. Nan, X. Xiao, Interfacial bonding of hydroxyl-modified g- C_3N_4 and $\text{Bi}_2\text{O}_2\text{CO}_3$ toward boosted CO_2 photoreduction: insights into the key role of OH groups, *Chem. Eng. J.* 452 (2023) 139191, <https://doi.org/10.1016/j.cej.2022.139191>.
- [26] Y. Luo, A. Zheng, J. Li, Y. Han, M. Xue, L. Zhang, Z. Yin, C. Xie, Z. Chen, L. Ji, Z. Hong, X. Xie, Integrated adsorption and photodegradation of tetracycline by bismuth oxycarbonate/biochar nanocomposites, *Chem. Eng. J.* 457 (2023) 141228, <https://doi.org/10.1016/j.cej.2022.141228>.
- [27] D. Li, P. Yu, X. Zhou, J.-H. Kim, Y. Zhang, P.J.J. Alvarez, Hierarchical $\text{Bi}_2\text{O}_2\text{CO}_3$ wrapped with modified graphene oxide for adsorption-enhanced photocatalytic inactivation of antibiotic resistant bacteria and resistance genes, *Water Res.* 184 (2020) 116157, <https://doi.org/10.1016/j.watres.2020.116157>.
- [28] S. Noamani, S. Niroomand, M. Rastgar, M. Sadrzadeh, Carbon-based polymer nanocomposite membranes for oily wastewater treatment, *NPJ Clean. Water* 2 (2019) 20, <https://doi.org/10.1038/s41545-019-0044-z>.
- [29] H. Han, B. Wang, Q. Tang, S. Jia, J. Liu, H. Li, C. Wang, H. Xu, Y. Hua, Non-metallic nitrogen-doped graphene quantum dots coupled with g- C_3N_4 achieve efficient photocatalytic performance, *Appl. Surf. Sci.* 649 (2024) 159171, <https://doi.org/10.1016/j.apsusc.2023.159171>.
- [30] J. Liu, S. Zhu, B. Wang, R. Yang, R. Wang, X. Zhu, Y. Song, J. Yuan, H. Xu, H. Li, A candy-like photocatalyst by wrapping Co, N-co-doped hollow carbon sphere with ultrathin mesoporous carbon nitride for boosted photocatalytic hydrogen evolution, *Chin. Chem. Lett.* 34 (2023) 107749, <https://doi.org/10.1016/j.cclet.2022.107749>.
- [31] L. Ding, Z. Li, R. Liu, Y. Li, G. Yang, Z. Kang, B. Yang, M. Deng, H. Sun, Fabrication of electron's path based on carbonized polymer dots to accelerate photocatalytic hydrogen production kinetic for carbon nitride, *Appl. Catal. B* 334 (2023) 122806, <https://doi.org/10.1016/j.apcatb.2023.122806>.
- [32] J. Dong, J. Zhao, X. Yan, L. Li, G. Liu, M. Ji, B. Wang, Y. She, H. Li, J. Xia, Construction of carbonized polymer dots/potassium doped carbon nitride nanosheets van der Waals heterojunction by ball milling method for facilitating photocatalytic CO_2 reduction performance in pure water, *Appl. Catal. B* 351 (2024) 123993, <https://doi.org/10.1016/j.apcatb.2024.123993>.
- [33] B. Wang, J. Zhao, H. Chen, Y. Weng, H. Tang, Z. Chen, W. Zhu, Y. She, J. Xia, H. Li, Unique Z-scheme carbonized polymer dots/ $\text{Bi}_4\text{O}_5\text{Br}_2$ hybrids for efficiently boosting photocatalytic CO_2 reduction, *Appl. Catal. B* 293 (2021) 120182, <https://doi.org/10.1016/j.apcatb.2021.120182>.
- [34] B. Wang, J. Di, L. Lu, S. Yan, G. Liu, Y. Ye, H. Li, W. Zhu, H. Li, J. Xia, Sacrificing ionic liquid-assisted anchoring of carbonized polymer dots on perovskite-like PbBiO_2Br for robust CO_2 photoreduction, *Appl. Catal. B* 254 (2019) 551–559, <https://doi.org/10.1016/j.apcatb.2019.04.068>.
- [35] M. Han, C. Kang, Z. Qu, S. Zhu, B. Yang, Surface molecule induced effective light absorption and charge transfer for H_2 production photocatalysis in a carbonized polymer dots-carbon nitride system, *Appl. Catal. B* 305 (2022) 121064, <https://doi.org/10.1016/j.apcatb.2022.121064>.
- [36] J.P. Perdew, K. Burke, M. Ernzerhof, Generalized gradient approximation made simple, *Phys. Rev. Lett.* 77 (1996) 3865, <https://doi.org/10.1103/PhysRevLett.77.3865>.
- [37] G. Kresse, D. Joubert, From ultrasoft pseudopotentials to the projector augmented-wave method, *Phys. Rev. B* 59 (1999) 1758, <https://doi.org/10.1103/PhysRevB.59.1758>.
- [38] P.E. Blöchl, Projector augmented-wave method (<https://doi.org/>), *Phys. Rev. B* 50 (1994) 17953, <https://doi.org/10.1103/PhysRevB.50.17953>.
- [39] B. Wang, X. Zhu, F. Huang, Y. Qian, G. Liu, X. Zhang, F. Xiong, C. Huang, M. Ji, H. Li, P.K. Chu, J. Xia, Porous edge confinement: High carrier potential and low activation energy barrier synergistically boosting the efficiency of selective photocatalytic CO_2 conversion, *Appl. Catal. B* 325 (2023) 122304, <https://doi.org/10.1016/j.apcatb.2022.122304>.
- [40] T. Xiong, W. Cen, Y. Zhang, F. Dong, Bridging the g- C_3N_4 interlayers for enhanced photocatalysis, *ACS Catal.* 6 (2016) 2462–2472, <https://doi.org/10.1021/acscatal.5b02922>.
- [41] W.S. Cho, D.M. Hong, W.J. Dong, T.H. Lee, C.J. Yoo, D. Lee, H.W. Jang, J.-L. Lee, Porously reduced 2-dimensional $\text{Bi}_2\text{O}_2\text{CO}_3$ petals for strain-mediated electrochemical CO_2 Reduction to HCOOH , *Energy Environ. Sci.* 0 (2022) e12490, <https://doi.org/10.1002/eeem.2.12490>.
- [42] J. Liu, H. Xu, Y. Xu, Y. Song, J. Lian, Y. Zhao, L. Wang, L. Huang, H. Ji, H. Li, Graphene quantum dots modified mesoporous graphite carbon nitride with significant enhancement of photocatalytic activity, *Applied Catalysis B: Environmental* 207 (2017) 429–437, <https://doi.org/10.1016/j.apcatb.2017.01.071>.
- [43] Z. Jin, H. Li, J. Li, Efficient photocatalytic hydrogen evolution over graphdiyne boosted with a cobalt sulfide formed S-scheme heterojunction, *Chin. J. Catal.* 32 (2022) 2202885, [https://doi.org/10.1016/s1872-2067\(21\)63818-4](https://doi.org/10.1016/s1872-2067(21)63818-4).
- [44] B. Wang, W. Zhang, G. Liu, H. Chen, Y. Weng, H. Li, P.K. Chu, J. Xia, Excited electron-rich $\text{Bi}^{(3-x)+}$ sites: a quantum well-like structure for highly promoted selective photocatalytic CO_2 reduction performance, *Adv. Funct. Mater.* 32 (2022) 2202885, <https://doi.org/10.1002/adfm.202202885>.
- [45] L. Ye, X. Jin, X. Ji, C. Liu, Y. Su, H. Xie, C. Liu, Facet-dependent photocatalytic reduction of CO_2 on BiOI nanosheets, *Chem. Eng. J.* 291 (2016) 39–46, <https://doi.org/10.1016/j.cej.2016.01.032>.
- [46] J. Li, M. Li, Y. Li, X. Guo, Z. Jin, Lotus-leaf-like $\text{Bi}_2\text{O}_2\text{CO}_3$ nanosheet combined with Mo_2S_3 for higher photocatalytic hydrogen evolution, *Sep. Purif. Technol.* 288 (2022) 120588, <https://doi.org/10.1016/j.seppur.2022.120588>.
- [47] Y. Dai, C. Li, Y. Shen, T. Lim, J. Xu, Y. Li, H. Niemantsverdriet, F. Besenbacher, N. Lock, R. Su, Light-tuned selective photosynthesis of azo-and azoxy-aromatics using graphitic C_3N_4 , *Nat. Commun.* 9 (2018) 60, <https://doi.org/10.1038/s41467-017-02527-8>.
- [48] T.K. Nguyen, T.-T. Pham, B. Gendensuren, E.-S. Oh, E.W. Shin, Defect engineering of water-dispersible g- C_3N_4 photocatalysts by chemical oxidative etching of bulk g- C_3N_4 prepared in different calcination atmospheres, *J. Mater. Sci. Technol.* 103 (2022) 232–243, <https://doi.org/10.1016/j.jmst.2021.07.013>.
- [49] K. Li, Y. Lin, K. Wang, Y. Wang, Y. Zhang, Y. Zhang, F. Liu, Rational design of cocatalyst system for improving the photocatalytic hydrogen evolution activity of graphite carbon nitride, *Appl. Catal. B* 268 (2020) 118402, <https://doi.org/10.1016/j.apcatb.2019.118402>.
- [50] D. Gao, J. Xu, L. Wang, B. Zhu, H. Yu, J. Yu, Optimizing atomic hydrogen desorption of sulfur-rich NiS_{1+x} cocatalyst for boosting photocatalytic H_2 evolution, *Adv. Mater.* 34 (2022) 2108475, <https://doi.org/10.1002/adma.202108475>.
- [51] T. Huang, J.Q. Chen, L.L. Zhang, A. Khataee, Q.F. Han, X.H. Liu, J.W. Sun, J. W. Zhu, S.G. Pan, X. Wang, Y.S. Fu, Precursor-modified strategy to synthesize thin porous amino-rich graphitic carbon nitride with enhanced photocatalytic degradation of RhB and hydrogen evolution performances, *Chin. J. Catal.* 43 (2022) 497–506, [https://doi.org/10.1016/S1872-2067\(21\)63873-1](https://doi.org/10.1016/S1872-2067(21)63873-1).
- [52] B. Xia, B. He, J. Zhang, L. Li, Y. Zhang, J. Yu, J. Ran, S. Qiao, $\text{TiO}_2/\text{FePS}_3$ S-scheme heterojunction for greatly raised photocatalytic hydrogen evolution, *Adv. Energy Mater.* 12.46 (2022) 2201449, <https://doi.org/10.1002/aenm.202201449>.
- [53] H.J. Dong, X.X. Zhang, J.M. Li, P.J. Zhou, S.Y. Yu, N. Song, C.B. Liu, G.B. Che, C. M. Li, Construction of morphology-controlled nonmetal 2D/3D homojunction, *Appl. Catal. B* 263 (2020) 118270, <https://doi.org/10.1016/j.apcatb.2019.118270>.
- [54] Z. Qin, H. Sun, Y. Tang, Z. Chang, S. Yin, Z. Liu, Bio-inspired hierarchical assembly of Au/ZnO decorated carbonized spinach leaves with enhanced photocatalysis performance, *J. Alloy. Compd.* 829 (2020) 154393, <https://doi.org/10.1016/j.jallcom.2020.154393>.
- [55] S. Li, J. Hu, Photolytic and photocatalytic degradation of tetracycline: effect of humic acid on degradation kinetics and mechanisms, *J. Hazard. Mater.* 318 (2016) 134–144, <https://doi.org/10.1016/j.jhazmat.2016.05.100>.
- [56] M. Li, D. Wei, H. Zhao, Y. Du, Genotoxicity of quinolones: substituents contribution and transformation products QSAR evaluation using 2D and 3D models, *Chemosphere* 95 (2014) 220–226, <https://doi.org/10.1016/j.chemosphere.2013.09.002>.
- [57] T. Paul, M.C. Dodd, T.J. Strathmann, Photolytic and photocatalytic decomposition of aqueous ciprofloxacin: Transformation products and residual antibacterial activity, *Water Res.* 44 (2010) 3121–3132, <https://doi.org/10.1016/j.watres.2010.03.002>.
- [58] J. Zai, F. Cao, N. Liang, K. Yu, Y. Tian, H. Sun, X. Qian, Rose-like I-doped $\text{Bi}_2\text{O}_2\text{CO}_3$ microspheres with enhanced visible light response: DFT calculation, synthesis and photocatalytic performance, *J. Hazard. Mater.* 321 (2017) 464–472, <https://doi.org/10.1016/j.jhazmat.2016.09.034>.
- [59] G. Liu, L. Li, B. Wang, N. Shan, J. Dong, M. Ji, W. Zhu, P. Chu, J. Xia, H. Li, Construction of Bi nanoparticles loaded biocl nanosheets ohmic junction for photocatalytic CO_2 reduction, *Acta Phys.-Chim. Sin.* 40 (2024) 2306041, <https://doi.org/10.3866/PKU.WHXB202306041>.
- [60] Y. Peng, X. Guo, S. Xu, Y. Guo, D. Zhang, M. Wang, G. Wei, X. Yang, Z. Li, Y. Zhang, F. Tian, Surface modulation of $\text{MoS}_2/\text{O-ZnIn}_2\text{S}_4$ to boost photocatalytic H_2 evolution, *J. Energy Chem.* 75 (2022) 276–284, <https://doi.org/10.1016/j.jechem.2022.06.027>.
- [61] B. Wang, H. Chen, W. Zhang, H. Liu, Z. Zheng, F. Huang, J. Liu, G. Liu, X. Yan, Y. Weng, H. Li, Y. She, P.K. Chu, J. Xia, Semimetallic Bismuthene with Edge-Rich Dangling Bonds: Broad-Spectrum-Driven and Edge-Confined Electron Enhancement Boosting CO_2 Hydrogenation Reduction, *Adv. Mater.* (2024) 2312676, <https://doi.org/10.1002/adma.202312676>.
- [62] X. Ma, X. Cui, Z. Zhao, M.A. Melo Jr., E.J. Robertsc, F.E. Osterloh, Use of surface photovoltage spectroscopy to probe energy levels and charge carrier dynamics in transition metal (Ni, Cu, Fe, Mn, Rh) doped SrTiO_3 photocatalysts for H_2 evolution from water, *J. Mater. Chem. A* 6 (2018) 5774–5781, <https://doi.org/10.1039/C7TA10934B>.
- [63] J. Tian, X. Cao, T. Sun, J. Fan, H. Miao, Zh Chen, D. Li, E. Liu, Y. Zhu, S-scheme $\text{Co}_3(\text{PO}_4)_2/\text{Twinned-Cd}_{0.5}\text{Zn}_{0.5}\text{S}$ homo-heterojunction for enhanced photocatalytic H_2 evolution, *Chem. Eng. J.* 471 (2023) 144587, <https://doi.org/10.1016/j.cej.2023.144587>.
- [64] X. Yan, B. Wang, J. Zhao, G. Liu, M. Ji, X. Zhang, P.K. Chu, H. Li, J. Xia, Hierarchical columnar $\text{ZnIn}_2\text{S}_4/\text{BiVO}_4$ Z-scheme heterojunctions with carrier highway boost photocatalytic mineralization of antibiotics, *Chem. Eng. J.* 452 (2023) 139271, <https://doi.org/10.1016/j.cej.2022.139271>.
- [65] J. Dong, S. Ji, Y. Zhang, M. Ji, B. Wang, Y. Li, Z. Chen, J. Xia, Construction of Z-Scheme $\text{MnO}_2/\text{BiOBr}$ Heterojunction for Photocatalytic Ciprofloxacin Removal and CO_2 Reduction, *Acta Phys.-Chim. Sin.* 39 (2023) 2212011, <https://doi.org/10.3866/PKU.WHXB202212011>.